# GAMMA-RAY SPECTROSCOPY AND MULTIPOLARITY MEASUREMENTS OF THE PROTON-RICH NUCLEUS 91RU

A THESIS SUBMITTED TO

THE GRADUATE SCHOOL OF NATURAL AND APPLIED SCIENCES

OF

MIDDLE EAST TECHNICAL UNIVERSITY

BY

ÖZGE AKTAŞ

IN PARTIAL FULFILLMENT OF THE REQUIREMENT

FOR

THE DEGREE OF MASTER OF SCIENCE IN

PHYSICS

AUGUST 2013

Approval of the thesis:

**GAMMA-RAY SPECTROSCOPY AND MULTIPOLARITY MEASUREMENTS OF THE PROTON-RICH NUCLEUS 91RU**

Submitted by **ÖZGE AKTAŞ** in partial fulfillment of the requirements for the degree of **Master of Science in Physics Department, Middle East Technical University** by,

Prof. Dr. Canan ÖZGEN _____
Dean, Graduate School of **Natural and Applied Sciences**

Prof. Dr. Mehmet ZEYREK _____
Head of Department, **Physics Department**

Prof. Dr. Osman YILMAZ _____
Supervisor, **Physics Department, METU**

Prof. Dr. Ayşe ATAÇ NYBERG _____
Co-Supervisor, **Physics Department, KTH Royal Institute of Technology**

**Examining Committee Members:**

Prof. Dr. Şakir AYIK _____
Physics Dept., Tennessee Univ., USA

Prof. Dr. Osman YILMAZ _____
Physics Dept., METU

Prof. Dr. Ayşe ATAÇ NYBERG _____
Physics Dept., KTH Royal Institute of Technology, Sweden

Prof. Dr. Ahmet GÖKALP _____
Physics Dept., Bilkent University

Prof. Dr. Gürsevil TURAN _____
Physics Dept., METU

**Date: 02.08.2013**

**I hereby declare that all information in this document has been obtained and presented in accordance with academic rules and ethical conduct. I also declare that, as required by these rules and conduct, I have fully cited and referenced all material and results that are not original to this work.**

Name, Last name: Özge Aktaş

Signature:

## ABSTRACT

### GAMMA-RAY SPECTROSCOPY AND MULTIPOLARITY MEASUREMENTS OF THE PROTON-RICH NUCLEUS 91RU

Aktaş, Özge

M.S., Department of Physics

Supervisor : Prof. Dr. Osman Yılmaz

Co-Supervisor : Prof. Dr. Ayşe Ataç Nyberg

August 2013, 52 pages

In this work, the γ rays emitted by the highly excited $^{91}$Ru nucleus are studied in order to investigate the structure of this nucleus. The nucleus was produced in a heavy-ion fusion evaporation reaction by using an $^{36}$Ar beam, at an energy of 111MeV, on a $^{58}$Ni target at the GANIL facility in France. The DIAMANT and Neutron Wall detector arrays were used to measure the charged particles and neutrons, which were evaporated after the heavy-ion reaction, and the EXOGAM HPGe detector array was used for measuring the emitted gamma rays. Six new gamma-ray transitions at 234 keV, 520 keV, 686 keV, 1280 keV, 1614 keV and 1660 keV energies were observed and located in the level scheme by using the gamma-ray coincidence technique. By making use of the special design of the EXOGAM detectors, the angular correlation and linear polarization of gamma rays were measured in order to make firm spin and parity assignments to the excited nuclear states. One new nuclear state was found at an energy of 1660 keV with a spin and parity of $(11/2)^+$. Furthermore, tentative spin and parity values of the previously known states were confirmed. The experimentally determined level scheme of $^{91}$Ru is in agreement with the previously performed shell model calculations.



Keywords: Gamma-ray spectroscopy, $^{91}$Ru, Proton-rich nucleus, Angular correlation, Linear Polarization, Asymmetry, $R_{DCO}$

# ÖZ

## PROTON ZENGİNİ 91RU ÇEKİRDEĞİNİN GAMA-IŞIN TAYFÖLÇÜMÜ VE ÇOK KUTUPLULUK ÖLÇÜMÜ

Aktaş, Özge

Master, Fizik Bölümü

Tez Yöneticisi : Prof. Dr. Osman Yılmaz

Ortak Tez Yöneticisi : Prof. Dr. Ayşe Ataç Nyberg

Ağustos 2013, 52 sayfa

Bu çalışma, $^{91}$Ru çekirdeği tarafından yayınlanan γ ışınlarının ölçülmesini ve çekirdeğin yapısının incelenmesini içermektedir. $^{91}$Ru çekirdeği, $^{58}$Ni hedefine 111 MeV enerjide $^{36}$Ar demeti gönderilmesiyle oluşan bileşik çekirdek reaksiyonu sonucunda, Fransa'da bulunan GANIL tesislerinde oluşturulmuştur. Reaksiyon sonucu atılan yüklü parçacık ve nötronlar DIAMANT ve Neutron Wall detektör sistemleri ile gama ışınları ise EXOGAM HPGe detektör sistemi ile ölçülmüşlerdir. Bu çalışma sırasında, 234 keV, 520 keV, 686 keV, 1280 keV, 1614 keV ve 1660 keV enerjilerde altı yeni gamma-geçişi gözlenmiştir. EXOGAM detektörlerinin özellikleri kullanılarak gama ışınları için açısal korelasyon ve doğrusal polarizasyon ölçümleri yapılmış, bu ölçüm sonuçları nükleer enerji durumlarının spin ve paritelerinin belirlenmesinde kullanılmıştır. Bu çalışmada, enerjisi 1660 MeV, spin ve paritesi $(11/2)^+$ olan yeni bir durum bulunmuştur. Yeni deneysel bulgular, daha önceki çalışmalarda geçici olarak belirlenen spin ve parite değerlerini doğrulamıştır. Son olarak, $^{91}$Ru çekirdeği için belirlenen durum şeması daha evvel yapılan Kabuk Model hesapları ile karşılaştırılmış ve deneysel sonuçların teorik beklentiler ile uyumlu olduğu belirlenmiştir.

Anahtar kelimeler: Gamma ışın tayf ölçümü, $^{91}$Ru, Proton zengini çekirdek, Açısal korelasyon, Doğrusal polarizasyon, Asimetri, $R_{DCO}$

To my parents,

*Rukiye* and *Cengiz AKTAŞ*

**ACKNOWLEDGEMENTS**

First and foremost, I would like to express my sincere gratitude to my co supervisor Prof. Dr. Ayşe Ataç Nyberg for her guidance, support, enthusiasm, valuable feedback and encouraging conversations we had throughout this study. Without her guidance and support, this study would never have been accomplished.

Furthermore, I would like to thank my supervisor Prof. Dr. Osman Yılmaz for his directions and guidance to study experimental nuclear physics, without his directions, I wouldn't have a chance to study this field. Also, I would like to thank to the participants of experiment for their efforts and works. I owe a debt of gratitude to my friends who supported me throughout the study, Dilber Demirtaş, Belkıs Garip, Özge Tabak and Tuğba Kamalı. I really appreciate their contribution to the study, without their psychological and physical support and endure my endless complaining's, this thesis wouldn't be finished this year.

Last but not least, I would like to express my deepest gratitude to my family; to my parents Rukiye and Cengiz Aktaş, to my dear sister Özlem Aktaş, and to my lovely brother Hüseyin Eren Aktaş for their unconditional love, continuous support, and guidance. I am proud to be a part of this family.

**TABLE OF CONTENTS**

## LIST OF FIGURES

## LIST OF TABLES

## ABBREVIATIONS

| | |
|---|---|
| **A** | Mass Number |
| **BC501A** | Saint-Gobain Crystals - Bicron Model:501A |
| **CsI (Tl)** | Cesium Iodide Doped With Thallium |
| **DCO** | Directional Correlation Of Oriented State |
| **GANIL** | Grand Accelerateur National d'Ions Lourds |
| **HPGe** | High purity Germanium |
| **ISOL** | Isotope Separation On-Line |
| **N** | Neutron Number |
| **NMS** | Nuclear Shell Model |
| **PID** | Particle Identification |
| **QVC** | Charge to Voltage |
| **SPIRAL** | Systéme de Production d'Ions Radioactifs en Linge |
| **TOF** | Time-Of-Flight |
| **Z** | Atomic Number (Proton Number) |
| **ZCO** | Zero Cross-Over |

# CHAPTER 1

## INTRODUCTION

Uranium was first discovered in 1789 by Martin Klaproth who named it after the planet Uranus. Later in 1895, Wilhelm Röntgen discovered ionizing radiation by using a system where electric current passing through an evacuated glass tube produced continuous X-rays. In the meanwhile, Henry Becquerel was studying X-rays from Uranium salts and unexpectedly, he found that Uranium salts emitted a new form of radiation, which were different from X-rays. He called the new type of radiation as Uranic rays. Actually, this phenomenon is now known as spontaneous radiation, and its discovery is accepted as the beginning of nuclear physics [1]. Later, a third type of radiation was observed from Uranium. This was γ-ray radiation which was nearly the same as X-ray radiation. In 1896 Maria and Pierre Curie began to investigate this phenomenon systematically and they found that such emissions were not unique for Uranium. They discovered Polonium and Radium in 1898. After these discoveries, the name 'radioactivity' was given to these phenomena. Four years later, in 1902 Ernest Rutherford found that matters like Uranium and Thorium transmute naturally into another elements, by spontaneous α and β decay. Few years later, Frederick Soddy discovered that naturally-radioactive elements had different isotopes with the same chemical properties. After Chadwick's discovery of neutron in 1932, scientist started using neutrons to create new artificial radionuclides. Today, the nuclear chart consists of a total of around 6000 nuclei, nearly 3000 of them are known and 300 of them are stable, see Fig. 1.1 [2].

The nuclear landscape shown in Fig. 1.1 is a two dimensional plot where the horizontal axis is the neutron number and vertical axis is the proton number. Nuclear landscape or chart is divided into three main areas. The black area represents the stability line or valley. Out of 300 stable nuclei, 168 of them have even number of protons and neutrons, whereas, only 4 have odd proton and neutron numbers. Up to A=40 the stability line follows the N=Z line, then it bends towards the neutron drip line. The reason of this bending is the repulsive Coulomb force. When the number of protons increase the effect of Coulomb force increases and to balance this, the attractive strong force between the nucleons should be increased by increasing the number of neutrons. The second region in the chart is the yellow area which contains the nuclei, which are mainly reached in the laboratories. There are nearly 3000 isotopes in this region. The nuclei with excess number of protons as compared to the ones which lie on the line of stability, are called proton rich nuclei. Similarly, we have neutron rich nuclei with an excess of neutrons above the stability line. The proton and neutron drip lines determine the limits of the nuclear chart. Above the proton drip line and below the neutron drip line, the proton and neutron binding energies become zero. Third region, "terra incognita" is marked

by green colour in the chart of nuclides. The nuclei in this region are unknown, however, they most likely existed in the universe at some stage. The astrophysical r- and rp- process lines are found in this region.

The structure of nuclei which lie close to the line of stability are well known and the nuclear models are developed based on our knowledge about these nuclei. There are two main nuclear models, liquid drop model and nuclear shell model (NSM). This thesis emphasizes on NSM and deformed shell model. Moving away from the line of stability towards the proton and neutron drip lines, the nuclear structure is less known. Therefore the nuclear models may need improvements. As an example the appearance of new magic numbers and the disappearance of the well-established ones are expected in this region [3, 4].

On the proton rich side, the nuclei around the doubly magic nucleus $^{100}$Sn (50 protons and 50 neutrons) are especially interesting since the protons and neutrons occupy the same shell model single particle states with same quantum numbers and they may form pairs. Indeed, in the neighboring nucleus $^{92}_{46}Pd_{46}$, evidence for neutron-proton coupling was recently observed [5]. This kind of couplings can also be observed in the neighboring nuclei and a systematic study of the region is required.

The experimental data set which is used in this work is the same as the one used for studying $^{92}_{46}Pd_{46}$. In this work, however, the neighboring $^{91}_{44}Ru_{47}$ nucleus was studied. Both nuclei are the daughter nuclei of compound nucleus $^{94}$Pd. The experiment was performed in 2010 at GANIL (Grand Accelerateur National d'Ions Lourds) facility. The reaction type is heavy –ion fusion evaporation reaction and created with bombarding $^{58}$Ni target with $^{36}$Ar beam at 111 MeV energy. For measuring the neutrons, charged particles which were emitted from the compound nucleus, Neutron wall and Diamant detector systems were used. The γ rays from the $^{91}$Ru nucleus were measured by the EXOGAM Ge detectors.

$^{91}$Ru nucleus has 44 protons and 47 neutrons and in the nuclear chart, it lies outside of the stability region, at the far edge of the yellow region. Because it is near to the doubly magic nucleus $^{100}$Sn, it is nearly spherical with a weak deformation. The A≈90 region is known as the transition region between deformed nuclei and spherical nuclei. First information about the level structure of $^{91}$Ru was published in 1993 by Arnell et al. [6] In that work, they used $^{40}$Ca beam at 187 MeV energy and $^{58}$Ni target was used with NORDBALL detector system. In this work, many excited states of the nucleus were found. They made tentative spin and parity assignments to the nuclear levels. One years later, in 1994 J. Heese et al. [7] studied the same nucleus with a different reaction. They used $^{36}$Ar beam at 146 MeV energy with $^{58}$Ni target and OSIRIS spectrometers to measure γ-rays. The aim of this paper was to find agreement between the experimental results and the theory. They found out that the experimental results agree well with the theoretical shell model calculations.

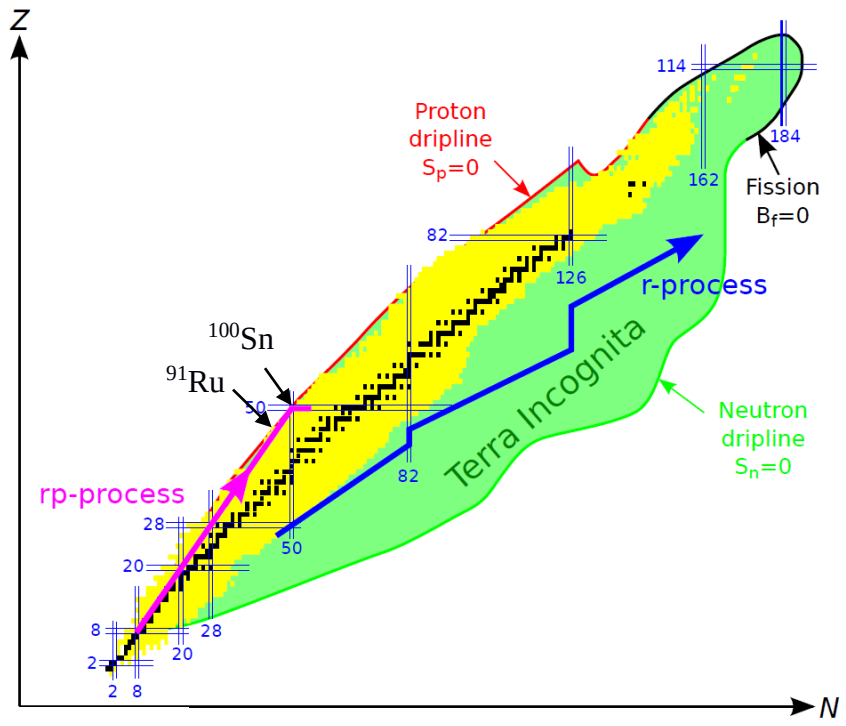


Figure 1.1: The chart of nuclides. The black points represent stable nuclei and they form the line of stability. The yellow area marks the known nuclei whereas the green area represents unknown nuclei which are predicted in the theories. Double blue lines show the place of magic numbers of the nuclear shell model. The locations of $^{91}$Ru and $^{100}$Sn nuclei are marked in the figure. This figure is taken from ref. [2] .

The aim of this thesis work, was to improve the level scheme of $^{91}$Ru and to make new spin and parity assignments. These assignments were made by using methods which were based on angular correlations and linear polarizations of emitted γ rays. With the special design of the EXOGAM γ-ray detectors, it was possible to measure the polarization of Compton scattered γ rays which were emitted from the $^{91}$Ru nucleus. The newly observed γ-ray transitions and new nuclear states are already published by the group of researchers that includes also the writer of this thesis [8]. In the close future the new states will be compared to the theoretical calculations performed by using the NSM.

This thesis consists of six chapters. First chapter is the introduction chapter, the chart of nuclides and the aim of the thesis is explained. There is also a brief information about the earlier work on $^{91}$Ru. In the second chapter nuclear reactions and experimental techniques are explained. In this chapter, the heavy ion fusion evaporation reaction, experimental setup and data analysis apparatus are explained. Third chapter is the theoretical overview. The NSM and deformed shell model are mentioned. Also the results of deformed shell model calculations for $^{91}$Ru from ref. [7] is given to compare with experimental results. Fourth chapter contains the properties of γ-ray transitions. First three main interactions of γ rays with matter are explained then the γ-ray transition and selection rules are mentioned with transition

probabilities. Also the angular distribution and polarization of γ-ray measurements methods are explained. The results of this work are explained in the fifth chapter where the new γ-ray transitions of $^{91}$Ru, and spin and parity assignments for newly observed and already known nuclear states are given. The least chapter gives the summary and the conclusions for this thesis.

# CHAPTER 2

# NUCLEAR REACTION AND EXPERIMENTAL TECHNIQUE

For studying γ-ray transitions from the $^{91}$Ru nucleus, one should first form the excited nucleus by a nuclear reaction. Usually, one simulates the reaction beforehand, in order to check the reaction cross sections and to decide about the beam energy. In this work, a heavy-ion fusion evaporation reaction was used to study the $^{91}$Ru nucleus. In this section, the fusion evaporation is explained and some information about the experimental set-up, detectors, data sorting and analysis is given in this order.

## 2.1 Heavy-Ion Fusion Evaporation Reaction

This reaction consists of two steps, the first step is the production of a compound nucleus which lives for about $10^{-18}$ s. The compound system is hot, which means that it has high excitation energy and it is rotating rapidly. The angular momentum of this system can be as large as 50 ħ -80 ħ [9]. In order to reduce the temperature it decays by the evaporation of α particles, protons and neutrons, during the second step. These particles carry away energy and angular momentum. However, due to the centrifugal barrier, the particles do not carry high angular momentum. Finally, the residual nucleus which is in excited state and has high angular momentum, is reached. It de-excites to the ground state by emitting a cascade of γ-rays which carry away both energy and angular momentum. The kinetic energy of the beam in the center of mass frame is a very important issue for producing the residual nuclei of interest. The schematic view of the production of compound nucleus $^{94}$Pd* and the possible daughter nuclei are represented in Fig. 2.1.

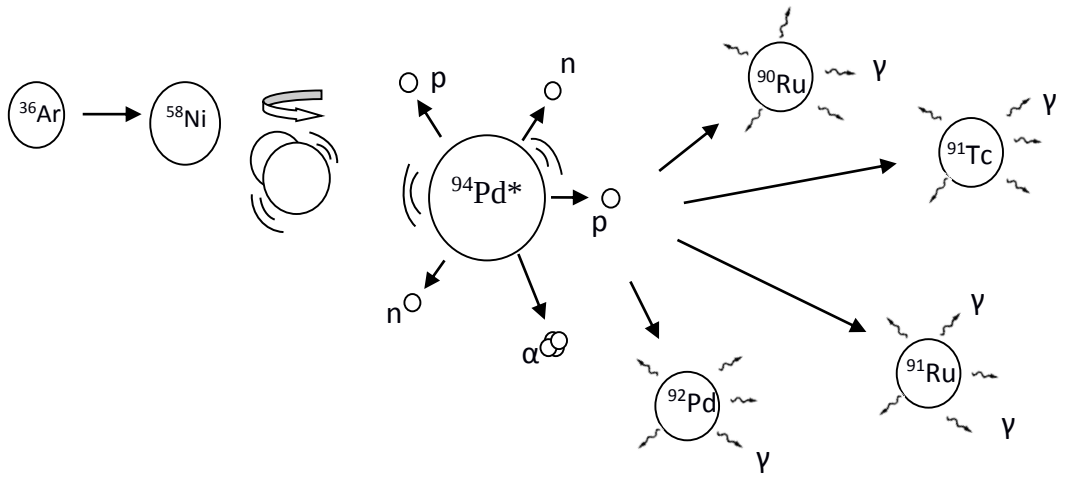


Figure 2.1: A schematic representation of the $^{58}$Ni+$^{36}$Ar fusion evaporation reaction.

The main aim of our experiment was to study the $^{92}$Pd nucleus, which had no known excited states before this experiment. The beam energy and target thickness were chosen to optimize the production of this nucleus. A high beam energy with thicker target could produce this nucleus with higher cross sections but the other strong reaction channels would then also increase and this would affect the quality of γ-ray energy spectra of $^{92}$Pd nucleus. Therefore, for producing $^{92}$Pd in 2n evaporation reaction channel, the beam energy should be arranged in such a way that it should be only slightly higher than the Coulomb barrier. The stopping power of the target at this energy was also calculated and taken into consideration. Finally, the energy of the $^{36}$Ar beam was 111 MeV and the intensity of it was 10 particle-nA ($6.10^{10}$ ions/second). The target is made of 99.8% isotropically enriched $^{58}$Ni with an areal density (thickness) of 6.0μg/cm$^2$.

### 2.1.1 Accelerator

The accelerator facility Spiral at GANIL (Grand Accelerateur National d'Ions Lourds) France was used for the experiment. GANIL is one of the five largest laboratories in the world for research using ion beams [10] SPIRAL is multi-beam facility with 5 cyclotrons and one can run up to six experiments simultaneously, in different experimental areas. During this experiment, the cyclotron CIME (Cyclotron pour Ions de Moyenne Energie, or Cyclotron for Ions of Medium Energy) particle accelerator was used. To create ion beam first step is to create source of ions. Since atoms have no electric charge, acceleration process is difficult so in order to ionize these atoms generally two main method is used. First one is generating electromagnetic fields using magnets to excited and released electrons so that the ions are created. Second method is heated atoms in some kind of oven at a temperature of approximately 1500 $^o$C and electrons energy is increased and escape from atom. Finally from both methods ion plasma is created. Then this plasma is focused with magnets and send to

cyclotron for acceleration process. The maximum intensity of $^{36}Ar^{+18}$ beam for this facility is 24 particle-μA and $800x10^{10}$ particle per second [11]. And for this experiment the desired intensity was 10 particle-nA and $6.10^{10}$ ions/second.

To accelerate the ions there are 5 different CIME cyclotrons for different energies. SPIRAL has two separated sector cyclotrons (CSS) which are composed of four magnets and generates a magnetic fields up to 4 Tesla. For this experiment CSS2 was used, CSS2 is known as high energy beam cyclotron and the energy of $^{36}Ar$ beam is 111 MeV. The accelerator send beams in bunches, and one bunch had a full width half maximum of around 3.5 ns. This bunches is used as a time reference for the trigger systems.

## 2.2 Detectors

For this experiment, multi- detector array systems were used. There were three different detector systems with different capabilities. The experimental set-up is shown in Fig. 2.2. For the charged particle detection, DIAMANT detectors were used in the inner shell of the detecting system. The NEUTRON WALL was covering 1π solid angle in the forward direction, was used to detect neutrons which evaporated from the reaction. EXOGAM detectors were located at $90^0$ relative to the beam axis and at backward angles and were used to detect γ rays.

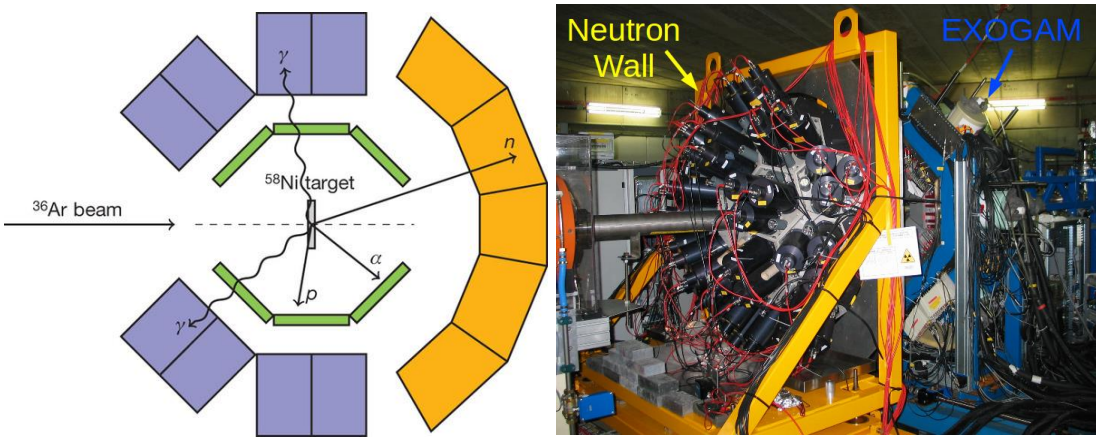


Figure 2.2: The schematic view of detector system, the real photography of detector system Neutron wall and Exogam [12]

### 2.2.1 Ancillary detectors: NEUTRON-WALL and DIAMANT

NEUTRON WALL (N-wall) was built in 1995-97 in GANIL to be used with the EUROBALL γ-ray spectrometer. It consists of 50 liquid scintillator detectors (BC-501A), bunched in 15 hexagonal and 1 pentagonal units. The detector thickness is 15 cm and distance from the target is 51 cm. The detector angles with respect to the beam axis is $0^o$ to $60^o$. The energy range of neutron detection is 0.5 MeV to 10 MeV. For fusion evaporation reactions one neutron

efficiency is around 20-25 % and two-neutron efficiency is around 1-3%. Three parameters read out from the detector; Zero Cross Over (ZCO), Time of Flight (ToF) and Charge to Voltage (QVC). In ZCO they check the pulse shape and neutron has a different pulse shape than γ rays. For ToF, N-wall time resolution is less than 1ns and neutron detectors take time from an external time ref.. For this experiment the pulsations of beam from the accelerator provide a time ref. [13]. Thus, ZCO and ToF techniques are combined to discriminate neutrons from γ rays. The interaction time difference between neutrons and gammas is around 16ns. This leads to a highly efficient neutron-γ separation. The probability of misinterpreting γ rays as neutrons is less than 3% of the neutron detector signals. [5]

For the charged particles like protons and α particles, DIAMANT detector was used. DIAMANT consists of 80 pieces 3mm CsI (Tl) scintillators. It covers 90% of 4π solid angle. For the detected charged particles, DIAMANT gives three parameters, the energy, the time and the particle identification (PID). The proton detection efficiency is around 70% and alpha detention efficiency is around 50%. In Fig. 2.3, a picture showing DIAMANT and N-wall is given.

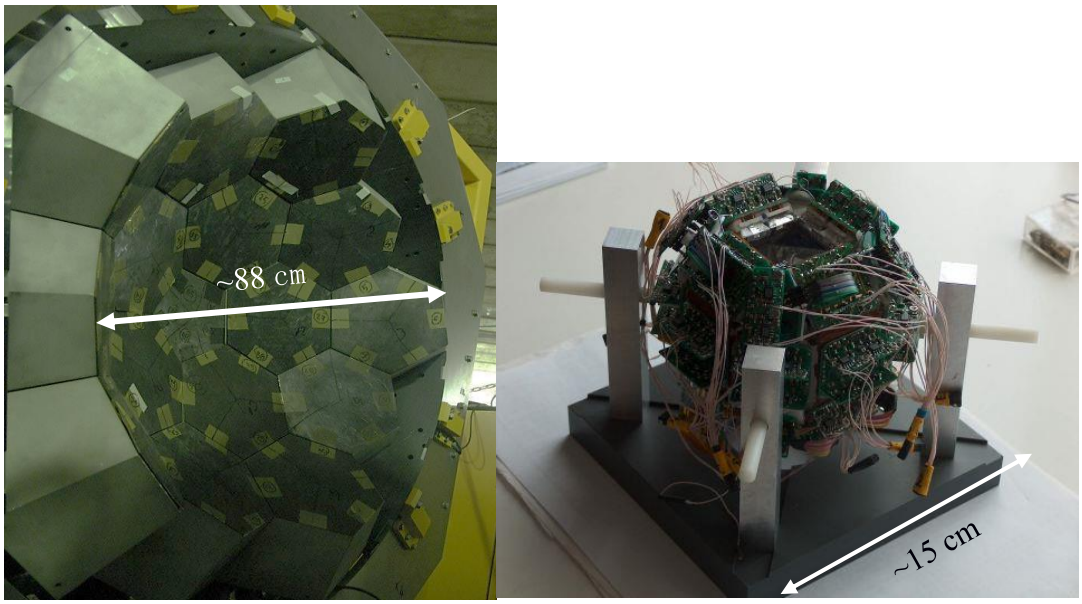


Figure 2.3: The photography of N-wall and Diamant detectors

### 2.2.2 Ge Detector EXOGAM

The emitted γ-rays from the evaporation reaction were detected by the EXOGAM Germanium detector array. EXOGAM is designed to maximize total photopeak efficiency for both low and high γ-ray energies. The specialty of the EXOGAM array is the modularity. It consist of 11 clover detectors. Each clover enclosed of four germanium crystals that were segmented

electronically to four equal regions, Fig. 2.4 (a). A segmented detector is a standard n-type semiconductor HPGe detector with 0.5 keV resolution signals. Adding scattered signals between the adjacent crystals enhances the efficiency. These signals carry the position and energy information. The total photo peak efficiency of EXOGAM is 11% at 1.3 MeV [12]. In order to suppress Compton background, Bismuth Germanate (BGO) escape suppress spectrometers were used in composite detectors. The front part of the BGO Compton suppression shields are removed to increase efficiency of γ ray detection. The schematic representation of clover germanium detectors with shields are shown in Fig. 2.4 b. Clover detectors are located in two different angles with respect to beam direction. Seven clover detectors were located at an angle of 90° and four of them at 135°.
The geometrical configuration of EXOGAM covers 3π solid angle and leaves 1π for the N-wall. A picture of the EXOGAM array is shown in Fig. 2.5 together with a schematic representation.

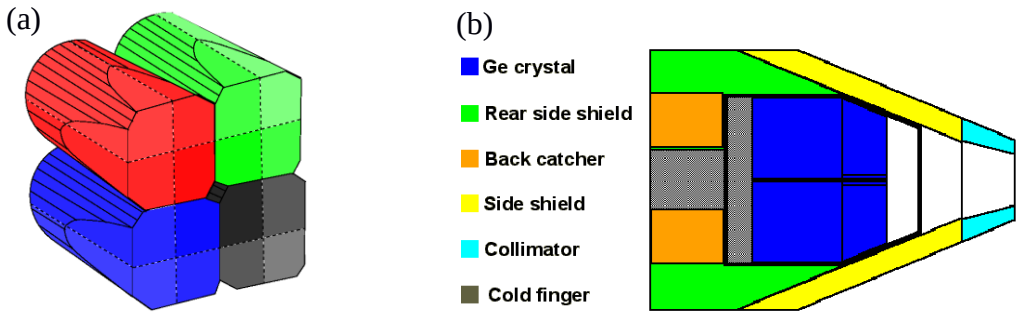


Figure 2.4: (a) Four Germanium crystals segmented electronically to four region in an EXOGAM clover. (b): Four cystals and the shielding for Compton suppression are shown.

So the EXOGAM detector signals give the position, the energy and the time information for each interacted γ ray. The clover form of the EXOGAM detectors and the electronically segmentation of HpGe crystals is very suitable to measure linear polarization of γ rays. In this work, we will make use of the clover form of the detectors and use the clover detectors as Compton polarimeter. This topic will be explained in sections. 4.3.2 and 5.2.2.

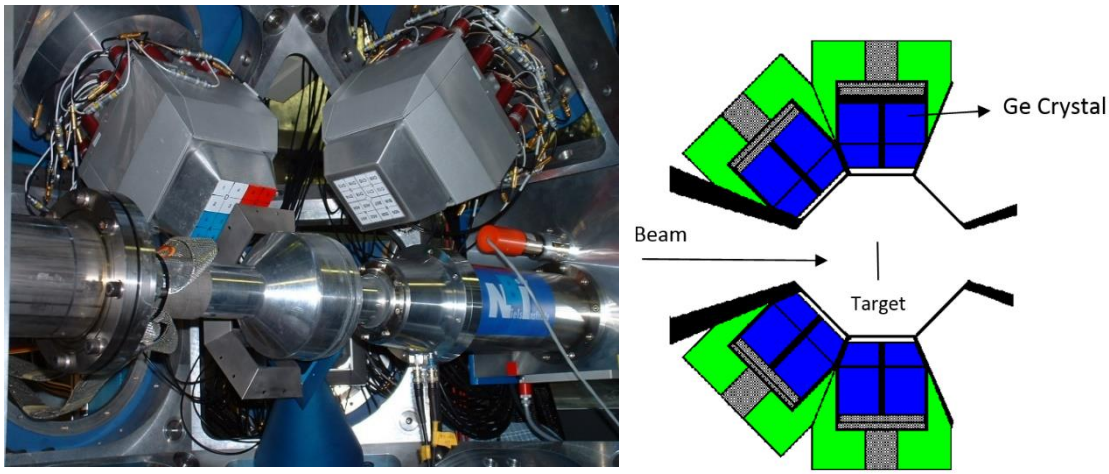


Figure 2.5: (a) The real image of EXOGAM at GANIL, (b) Schematic view of EXOGAM

## 2.3 Data analysis (trigger, sorting, gating)

Before the experiment, first the trigger system is arranged to activate data writings. For this experiment the trigger condition was set in such a way that one or more γ rays detected in EXOGAM with at least one neutron in N-wall detector will start the event. Therefore without neutron detection, the detected γ rays doesn't written as a valuable events. This condition was chosen in order to increase the percent of the reaction channels with neutron emission. Therefore all events that were recorded is 1 neutron gated. With this condition, in 14 days, 2.9x $10^9$ events were recorded in 563 files with maximum size of 700 Mbyte each.

When the experiment was running, by the help of the on-line analysis program, the quality of the spectra for each individual Ge, CsI (Tl) and Neutron detectors were checked. The calibration of energy spectra and efficiency measurements for the Ge detectors were done by using a $^{152}$Eu source. With the calibration parameters obtained by source measurements, Ge detectors were gain-matched in order to obtain good energy resolution. N-wall and Diamant calibrations were also important, especially for TOF discrimination of neutrons and γ-rays. The calibration of DIAMANT detectors was also done before and during the experiment and a good separation between protons and α-particles was obtained.

After the experiment, the γ-ray energies recorded by the Ge clover detectors were sorted into two dimensional histograms. This histograms were created with respect to proton, neutron and α particle decays. For the analysis of the $^{91}$Ru nucleus, two proton and one neutron condition was used and gamma-ray spectra were sorted with this condition. Therefore the deposited gammas in the histogram came after the 1 neutron and 2 proton decay process. The 1n2p reaction is the strongest one in all the events and 88% of the events is belong to the $^{91}$Ru nucleus [5].the total number of events in 1n2p gated histogram is 3x$10^7$. The software package RADWARE [14] was used to analyze the γ coincidence matrices. Especially gf3 and esc8tr programs were used to see and make measurements in coincidence γ-ray energies.

# CHAPTER 3

# THEORETICAL OVERVIEW

This part presents the physics background, and gives some theoretical predictions for $^{91}$Ru nucleus. Three out of the four basic forces are active in the atomic nuclei. These are the strong nuclear force, which is the attractive short range force that keeps the nucleons together, repulsive Coulomb force which acts between charged particles, protons and the weak force which is responsible for the β decay. The strong and weak nuclear forces are nucleon-nucleon forces and very complicated forces. With such a complicated nucleon-nucleon potential the meaningful solution for the many body problem is a difficult task. Therefore many phenomenological models have been developed to describe nucleus. Each model works well in different type of nuclear structures, or different nucleus.

These models are classified in two groups as the independent particle or single particle models and collective models. Collective models take nuclei as a whole without considering the individual nucleons. The most commonly used collective model is Liquid Drop Model (LDM) which is successful in explaining the motion of nuclei, like rotations and vibrations, where many of the nucleons contribute. Single particle models take nucleons as individual particles in the mean field potential. The most popular single particle model is Nuclear Shell Model (NSM). NSM has two different solutions for spherical nucleus and deformed nucleus. Spherical Shell model works well in spherical nuclei and describes correctly the magic numbers. However for deformed, non-spherical nucleus, NSM needs a modification for describing nuclear properties correctly, so Deformed Shell Model or Nilsson model works-well in this type of nuclei.

In this chapter the NSM and deformed shell model are explained. The research about $^{91}$Ru done by Heese et al. [7] shows that $^{91}$Ru nucleus is weakly deformed in transitional region of nuclei chart. Also $^{91}$Ru is very close the doubly magic $^{100}$Sn nucleus, which is well described by nuclear shell model. So the properties of $^{91}$Ru can be found by using nuclear shell model and Nilsson model. Especially $^{91}$Ru nuclear ground state and excited states; spin, parity and energies can be calculated with Nilsson model.

### 3.1 The Nuclear Shell Model

NSM predicts that nucleons, protons and neutrons, move freely in orbits in mean field potential without interaction. First information of shell structure comes from magic numbers. Magic numbers for nuclear physics are 2, 8, 20, 28, 50, 82, and 126 for both protons and neutrons. Magic nucleus has several common features such as, nucleus turns out to be especially stable, it has large total binding energy than the neighboring nuclei, single particle separation energy is larger than the neighboring nuclei, lowest excitation energy is higher than the normal ones, and the number of isotopes and isotones are higher than the other stable nuclei. This common features of magic numbers are main confirmation of shell structure in nuclei. For shell model, mean field potential has two main characteristics which are potential should be relatively constant inside the heavy nuclei and potential should go to zero outside the nuclear surface [15] [16]. There are three successful spherical symmetric potential that can be used in shell model. First one is Woods-Saxon potential, eqn 3.1, the potential depth $V_0$ is around 50 MeV, radius of nuclei is $R \approx 1.1 fm \, \mathrm{A}^{1/3}$, and surface thickness $a \approx 0.5 fm$. Although this potential gives shell structure it has a weakness that it cannot be used in obtaining analytical forms of wave function, it is used to determine the wave function numerically.

Second potential is square well potential, eqn. 3.2, and third potential is harmonic oscillator potential eqn. 3.3. These potentials have several disadvantages such as, they do not obey the nuclear limits, and they do not have scattering states. But they have analytical solutions and like all other potentials this give the first three magic numbers correctly.

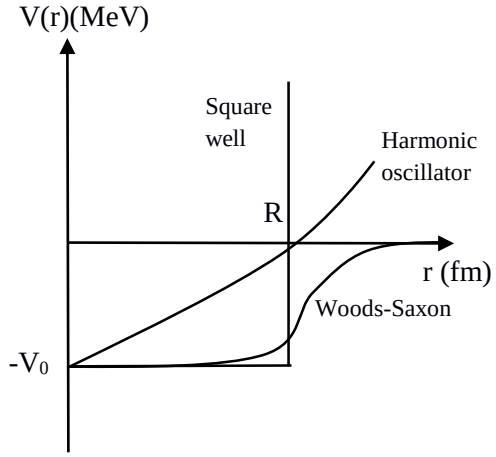


$$V(r) = \frac{-V_0}{1 + \exp\left[ (r - R)/a \right]} \tag{3.1}$$

$$V(r) = \begin{cases} -V_0 & \text{for } r \le R \\ \infty & \text{for } r > R \end{cases} \tag{3.2}$$

$$V(r) = \frac{1}{2} m \omega^2 r^2 \tag{3.3}$$

Figure 3.1: Sketch of three phenomenological shell model potentials.

By using a harmonic oscillator potential and solving the three-dimensional Schrödinger equation, the energy levels can be obtained as eqn. 3.4, depending on principle quantum number N. Each level has a degeneracy of $2(2\ell+1)$, where $\ell$ is represents the orbital angular

momentum. The factor of (2 $\ell$ +1) comes from $m_\ell$ degeneracy and 2 arises from the spin degeneracy $m_s$.

$$E_{n,\ell} = \left( N + \frac{3}{2} \right) \hbar\omega \ , \tag{3.4}$$

where $N = 2(n-1) + \ell$ , n=1,2,3….,∞ and n and ℓ are integers. In NSM, neutrons and protons are non-identical particles, which means 1s state can have 2 protons as well as 2 neutrons. Empirically it is assumed that there is an orbital splitting for different ℓ orbitals, written as:

$$E_{n,\ell} = \left( N + \frac{3}{2} \right) \hbar\omega + \mathrm{D}(\ell+1)\ell \, . \tag{3.5}$$

The constant D=-0.0225 ħω found from experimental data, the additional term just removes the states with different ℓ, to correct energy values, but there is still a problem in obtaining magic numbers.

Goeppert-Mayer and Jensen introduce a strong spin-orbit force to obtain magic numbers correctly. This force couples spin and orbital angular momentum of each individual nucleon, the additional term in single particle potential is $C.\hat{\ell} \cdot \hat{s}$ . Since $\hat{j} = \hat{\ell} + \hat{s}$ , $\langle \hat{\ell} \cdot \hat{s} \rangle$ is equal to $\frac{1}{2}\ell$ for $j = \ell + \frac{1}{2}$ and $-\frac{1}{2}(\ell+1)$ for $j = \ell - \frac{1}{2}$. Experimentally it is found that $j = \ell + \frac{1}{2}$ state is lower in energy so that the sign of C must be negative. Although there is a possibility to take C with r- dependency, because of the lack of experimental information we take it to be constant at -0.1ħω. By adding this term, all expected shell gaps are properly reproduced, eg. 28, 50, 82 and 126. This spin-orbit term breaks the degeneracy so that the energy now depends on three quantum numbers, *n*, $\ell$ and *j*. Each energy level has a degeneracy (2j + 1). In the Fig. 3.2, the final nucleon energy levels which are calculated with eqn 3.6, are shown as:

$$E = \left( N + \frac{3}{2} \right) \hbar\omega + \mathrm{D}\,(\ell+1)\ell + \mathrm{C}\,\hat{\ell} \cdot \hat{s} \, . \tag{3.6}$$

Moreover, apart from predicting the magic numbers, the NSM can also predict the parities and spins of ground and excited states and nuclear electromagnetic moments of the nuclei. The determination of nuclear ground state configuration and spin can be done in several different ways. The ground state is constructed by filling each state with protons and neutrons separately. For protons there is also coulomb interaction that lift energy levels above, but for the simple model we ignore coulomb interaction lifting and take neutron and proton levels as equal. For example, the nucleus with a number of n nucleons outside of the closed shell (magic nucleus) are supposed to determine the spin and parity of the nucleus. The shell that contains the extra nucleons or extra holes is called as a valence j-shell. Different combination for protons and neutrons as, nucleon-hole, hole-hole, and nucleon-nucleon combinations gives the spin and parity of the nuclear ground states. Although NSM works-well with magic numbers and define well the properties of spherical nuclei, for deformed (non-spherical) nucleus like

$^{91}$Ru, NSM predictions for ground state spin, energy, and parity is not correct. Deformed shell model is used for this type of nuclei.

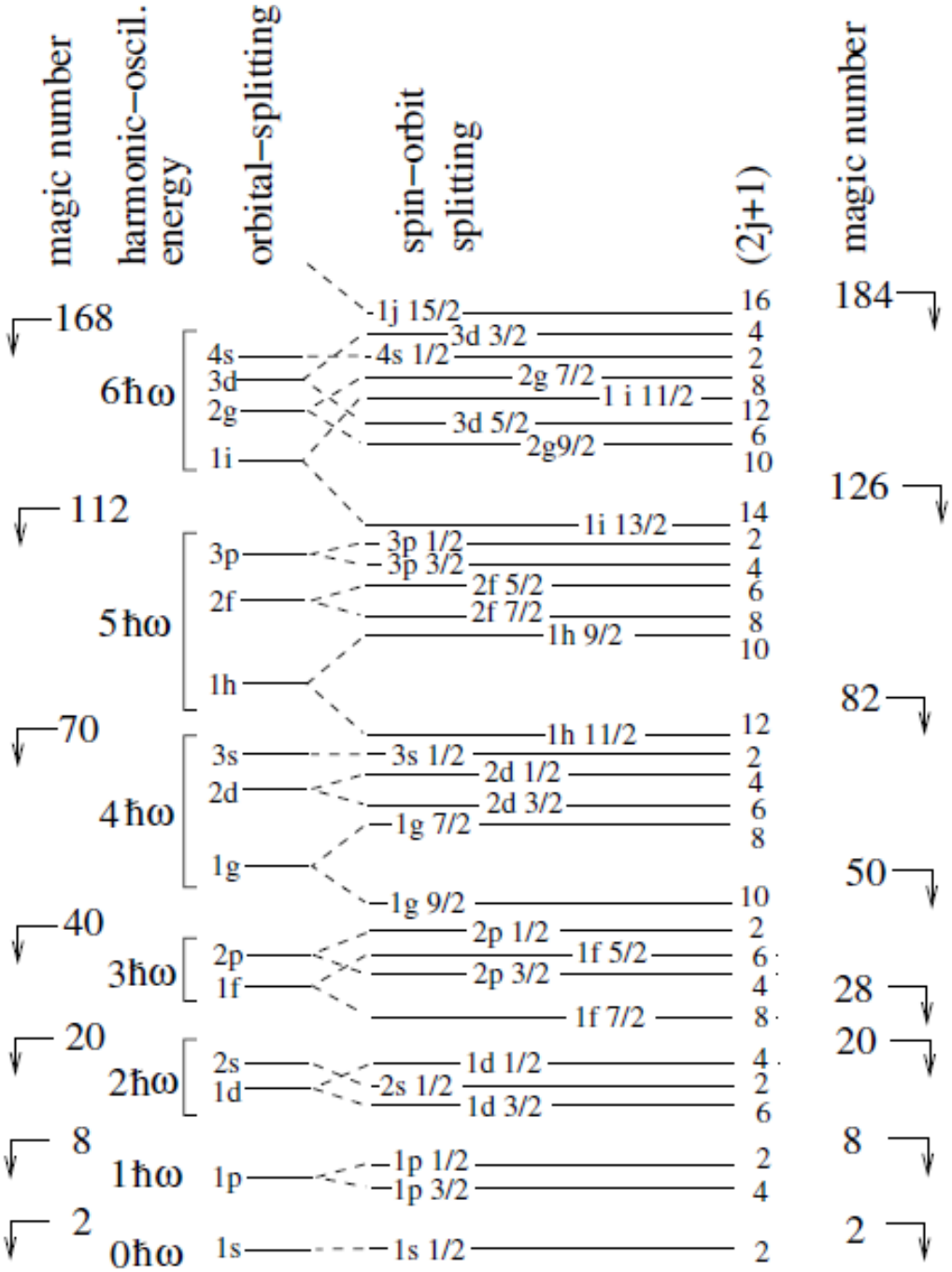


Figure 3.2 Nucleon energy levels before and after addition of the spin orbit coupling. This level scheme is taken from ref. [17].

### 3.2 Deformed Shell Model (Nilsson Model)

The aim of constructed new model is to generate independent particle wave function using deformed potentials. In deformed potential main idea is to make the oscillator constants different in the different spatial directions [16]. To decide this constants first of all one should decide nucleus shape and deformation type. In Nilsson model nucleus shape is taken as rotational ellipsoid. The deformed spherical harmonic oscillator potential can be written as:

$$V(r) = \frac{m}{2}\left(\omega_x^2 x^2 + \omega_y^2 y^2 + \omega_z^2 z^2\right). \tag{3.7}$$

The condition of incompressibility of nuclear matter requires that the volume of the ellipsoid be the same as that of the sphere, so the following conditions should be satisfied:

$$\omega_x \omega_Y \omega_z = \text{constant} \quad , \quad \omega_x^2 \omega_y^2 \omega_z^2 = \text{constant}. \tag{3.8}$$

To find oscillator frequencies, assume that axial symmetry is around the z axis, so $\omega_x = \omega_y$, and introduce a small deformation from spherical shape parameter δ, and the frequency $\omega_0$, then the frequencies are found as [15]:

$$\omega_x^2 = \omega_y^2 = \omega_0^2\left(1+\frac{2}{3}\delta\right) \quad , \quad \omega_z^2 = \omega_0^2\left(1-\frac{4}{3}\delta\right). \tag{3.9}$$

From the volume condition the $\omega_0\left(1-\frac{4}{3}\delta^2-\frac{16}{27}\delta^3\right)^{1/6}$ term is constant so $\omega_0$ is also constant. If these frequencies and conditions are substituted in the potential eqn. 3.7 the new form of the deformed potential is found as:

$$V(r) = \frac{1}{2}m\omega_0^2 r^2 - \beta_0 m\omega_0^2 r^2 Y_{20}(\theta,\phi) \tag{3.10}$$

where $Y_{20}$ is spherical harmonic function and $\beta_0$ is related to δ deformation value via

$$\beta_0 = \frac{4}{3}\sqrt{\frac{4\pi}{5}}\delta. \tag{3.11}$$

Using eqn. 3.10 and 3.11 the Hamiltonian of the system is:

$$H = -\frac{\hbar^2}{2M}\nabla^2 + \frac{1}{2}M\omega_0^2 r^2 - M\omega_0^2 r^2 \delta\frac{4}{3}\sqrt{\frac{\pi}{5}}Y_{20}(\theta,\phi) + C\hat{\ell}\cdot\hat{s} + D\hat{\ell}^2. \tag{3.12}$$

This Hamiltonian is the Nilsson Hamiltonian written in the form of a spherical symmetric shell model Hamiltonian with perturbation term. [15] To find the solution of Hamiltonian first we define the new quantum numbers for deformed nuclei. When the potential becomes non-spherical, $\ell$ is no longer a good quantum number, so the states cannot be identified with $\ell$ values. With the deformation one energy level become a mixture of the different $\ell$ values. In spherical case each state has (2j+1) degeneracy, however in a deformed nucleus this degeneracy is no longer true. In a deformed nucleus energy levels depend on the projection of

the j vector on the symmetry axis. There are 2j+1 possible components of projections that are symbolized by Ω, but there are (2j+1)/2 components because the positive +Ω and the negative -Ω give the same energy values. Hereby Ω =Σ+Λ is the total projection of the single particles angular momentum j on the symmetry axis, where Σ is projection of intrinsic spin s and Λ is the projection of orbital angular momentum $\ell$ along the symmetry axis. The vector representation is shown in Fig. 3.2. Also π represent the parity of the state which is expressed as $(-1)^N$. With these new asymptotic quantum numbers, Deformed Shell Model states are labelled as $\Omega^{\pi}$ [$Nn_z\Lambda$]. Here, for the total quantum number $N = n_x + n_y + n_z = n_\perp + n_z$.

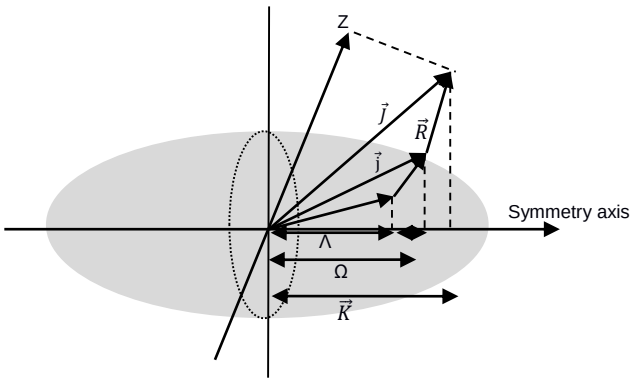


Figure 3.3 New asymptotic quantum numbers used in Deformed Shell Model.

These two deformation parameters δ and $\beta_0$ are related as eqn. 3.11. Negative values of δ and β parameters corresponds to an oblate shape. Positive δ and β parameters means that nucleus has a prolate shape. [18]

For the nucleus $^{91}$Ru that we are interested in this work, β and δ values are around 0.05 [19]. So, nucleus has a slightly deformed prolate shape. For prolate shapes, the state with the smallest Ω has the lowest energy.

In order to find the occupied single particle states and to determine the energy, spin and parity of the nuclear ground and excited states, we need to know the deformation $\beta$ value and we need to have a Nilsson diagram. To draw this diagram first the wave function should be found. The wave function of the Ω state, $\psi(\Omega)$ must be expressed as a combination of other states. Only limitation for mixture is parity, only the same parity states can be mixed. The mixed wave function is represented as $\psi'(\Omega)$, and $a(N\ell j)$ are the expansion coefficient which are depend on the deformation parameter δ, and calculated for each state by Nilsson [19].

$$\psi'(\Omega) = \sum_{\ell j} a\,(N\ell j)\,\psi_{N\ell j} \qquad (3.12)$$

These diagrams were first calculated by S. G. Nilsson in 1955. In Fig. 3.4 Nilsson diagram is shown where the single particle states are drawn as a function of nuclear deformations. These diagrams are very helpful to find angular momentum and parity of nucleus. The countdown

until the odd number of protons and neutrons in one state, was give the spin of the nucleus as I=Ω and the parity is the single particle state parity. As can be seen in fig.3.4 several levels are closed together at the deformation, in this case one of them gives the ground state properties and other quantum number combinations or nucleon occupation combinations gives other low-energy excitations.

### 3.2.1 $^{91}$Ru in a Simple Shell Model

For $^{91}$Ru the deformation parameter δ is around 0.05. So, the nucleus has a prolate shape, which is marked with red line in the Nilsson diagram. The ground state of $^{91}_{44}Ru_{47}$ was first identified by Komninos et al. [20] who assigned the state to have $I^{\pi} = 9/2^{+}$ in a $\beta^{+}$ + electron capture decay study. In a simple Shell Model, by only considering the last odd neutron at the nucleon state $1g_{9/2+}$, one can predict that the ground state of this nucleus should have $I^{\pi}=9/2^{+}$. This is in agreement with the experimental result.

Several NSM calculations were done for this nucleus. The first one was published in 1992 by Arnell [6] and the second one in 1994 by Heese [7]. Both of these studies used the semi magic nucleus $^{88}_{38}Sr_{50}$ as a core. In this case, $^{91}$Ru has 6 protons above Z=38 and three neutron holes below the N=50 shell closure. The restricted their model space to the $g_{9/2}$ and $p_{1/2}$ orbitals outside the semimagic core. The (+) and (-) parity states obtained by different configurations agreed quite well with the experimental results. The possible configurations and energies of these configurations can be found in ref. [7]. Their comparisons with the experimental results are shown in Fig. 3.5 for (+) and (-) parity states.

In a recent work by Zheng et al. [to be published] [8], a semi-empirical Shell Model was used, with known parameters from experimental data fits. In this calculation, the non-yrast states were investigated and newly observed states for example, the one located at 1660 MeV, was explained within the Shell Model.

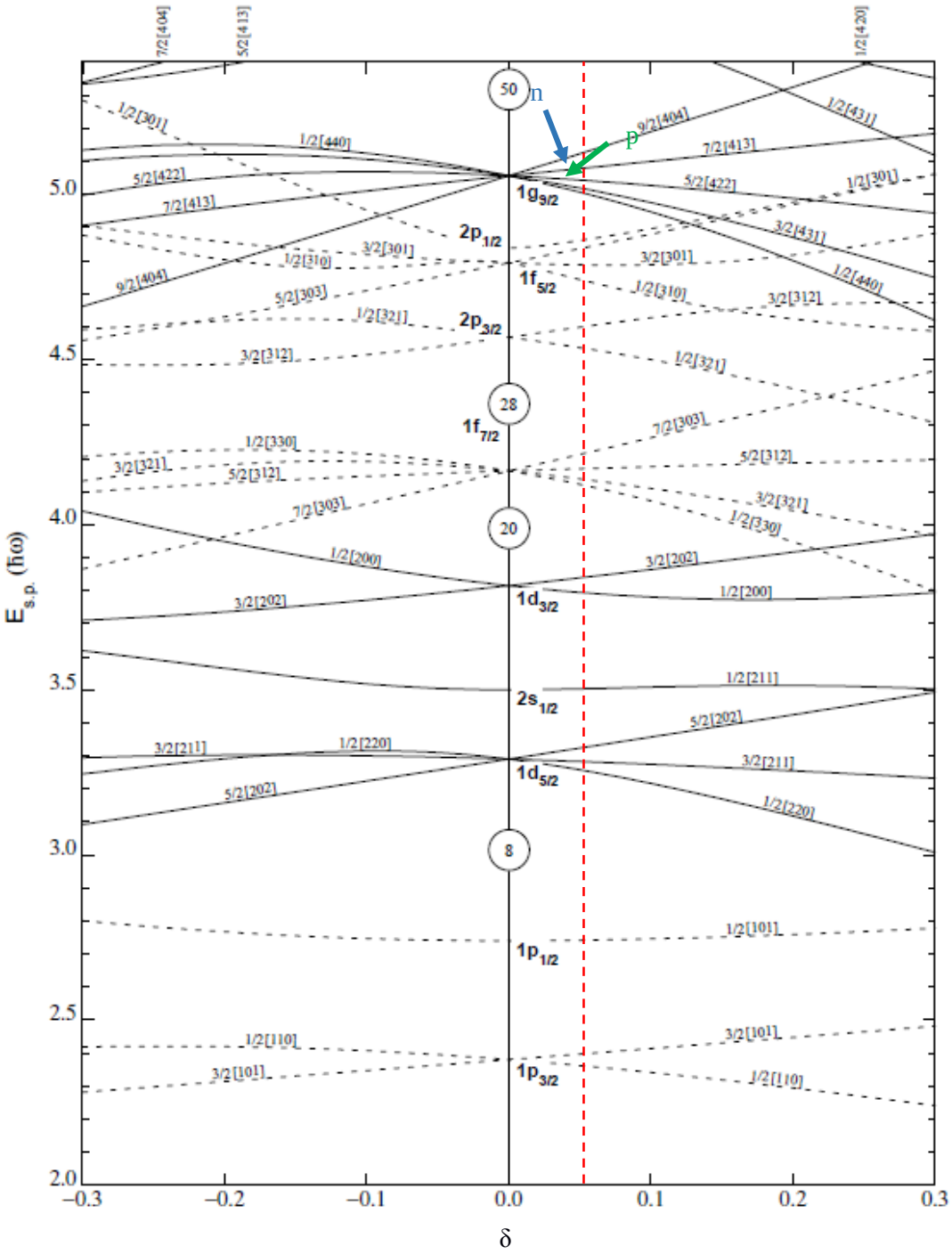


Figure 3.4 Nilsson diagram for proton and neutron numbers smaller than 50. The dashed lines represent the odd parity and continues lines represent the even parity levels. The red vertical line shows the δ region for the $^{91}$Ru nucleus. Blue arrow shows the last neutron level and green shows the last proton level.

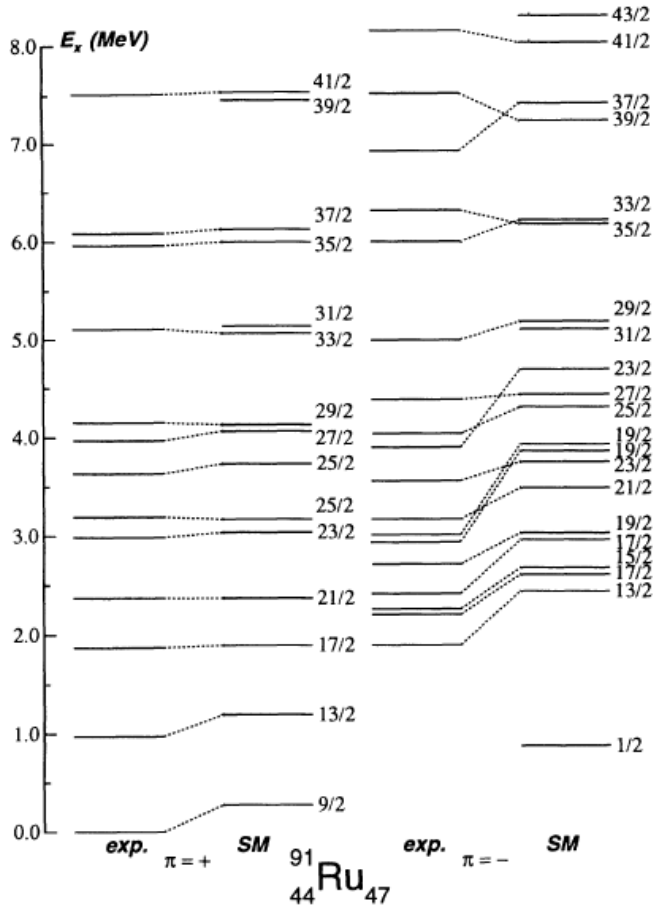


Figure 3.5 Comparison of experimental and calculated level energies in $^{91}$Ru. The predicted energies are normalized to the 21/2+ states [7].

# CHAPTER 4

# PROPERTIES OF GAMMA-RAY

Gamma ray is an electromagnetic radiation, has a short wavelength, typically below 10pm and has energy above 100 keV. It is also possible to describe the electromagnetic radiation as massless particles called photons. These gamma rays can be produced by the decay of a nucleus, through a transition from a high energy state to a low energy state and their properties depend on the properties of the initial and final nuclear states. In this section basic interactions of gamma rays with matter are summarized, and multipolarity, angular distribution and polarization of gamma-rays connecting the nuclear states are explained.

## 4.1 Interactions of Gamma-ray with Materia

There are various ways of gamma ray interactions with materials, but only the three of them has a significant role in gamma ray spectroscopy: Photoelectric absorption, Compton scattering and Pair production. With these processes a γ-ray transfers its energy partially or completely to an electron. These interaction mechanisms become dominant at different energy regions. For example, photoelectric absorption is dominant for low energy gamma-rays up to several hundred keV, pair production predominates for high energy gamma-rays above 5-10 MeV, and Compton scattering is the most probably process between several hundred keV energy to 5-10 MeV energy. However, energy is not the only important feature. The atomic number of the medium where interaction takes place, has also a strong influence on the probabilities of interactions. Figure 4.1 shows the cross sections for three interaction processes in Germanium, which is the material of EXOGAM detectors.

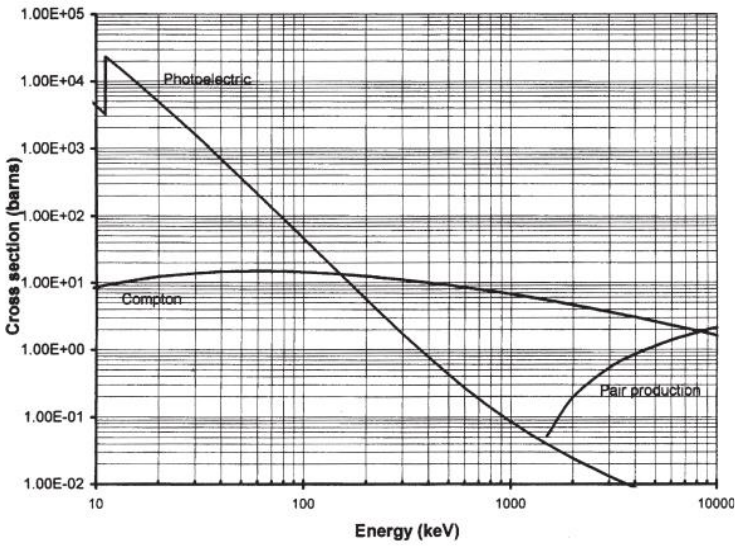


Figure 4.1 Compton, photoelectric and pair production cross sections for Germanium. [21]

### 4.1.1 Photoelectric Absorption

In the photoelectric absorption photon transfers whole its energy to an electron and it disappears completely. In this process, an energetic photoelectron is ejected by the atom from one of the shells. The photoelectron's kinetic energy is given by the incident photon energy, which is *hν* minus the binding energy *($E_b$)* of the electron. ($E_e = h\nu - E_b$) Photoelectric absorption process cannot take place with free electron because of energy conservation. This process is shown in the figure 4.2 below. For typical γ-ray energies, the photoelectron, most likely, emerges from the K shell of the atom.

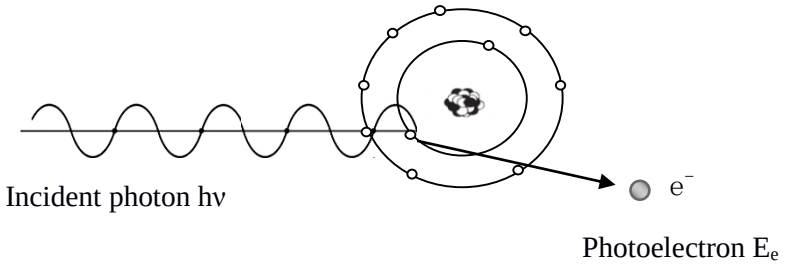


Figure 4.2 A schematic picture of the photoelectric effect.

With the emission of a photoelectron, a vacancy is created in the electron shell. The vacancy is immediately filled through capture of a free electron from a medium, or the rearrangement of electrons from other shells of the atom. Therefore one or two characteristic X-ray photons

may be generated, but generally this X-rays are reabsorbed by the photoelectric interactions with less tightly bound electron shells of the absorber atom. Alongside of X-ray photon generation, Auger electrons also can be created. Auger electron is the secondary product of rearrangements in electrons of the atom. In the rearrangements process the vacancy is filled by the other shell's electron and this replacement creates energy and with this energy one electron may be ejected from atom. This electron is secondary product and it is called as Auger electron, it has an extremely short range because it has low energy. Auger electron first observed by Australian physicist Lise Meitner in 1920, and discovered by French physicist Pierre Victor Auger in 1923. Observing an Auger electron is a rare event such as for iodine the X-ray ratio is %88 [18].

In the photoelectric absorption process, the emitted photoelectron carries most of the gamma-ray energy, together with one or more other low energetic electrons. If nothing escapes from the detector, then the total kinetic energy of the liberated electrons must give the total energy of the gamma-ray.

As mentioned before the photoelectric process is predominant in the low energy region, but the process is also dependent on the absorber materials atomic number Z. So the probability of photoelectric absorption can be roughly approximated as:

$$\tau \cong \text{constant} \times \frac{Z^n}{E_\gamma^{3.5}} \tag{4.1}$$

where $E_\gamma$ is the γ-ray energy. The exponent *n* varies between 4 and 5 over the gamma ray energy region of interest. This rough formula shows why the detectors are made of materials with high atomic numbers [22]. As a result photoelectric process is an ideal process to find the original gamma-ray energy.

### 4.1.2 Compton Scattering

The second mechanism that takes place between incident gamma ray and an electron in the absorbing material is Compton scattering. It is the most common interaction for typical γ-ray energies of radioisotope sources. The γ-ray transfers part of its energy to electron and new scattered photon is deflected, this process called Compton scattering. Compton scattering first observed by Arthur Holly Compton who received a Nobel Prize for physics in 1927 for its discovery. This interaction is illustrated in Fig. 4.3 where gamma-ray comes with energy *hv* transfers only a fraction of its energy to the electron and gamma- ray is deflected with θ angle and hν' energy. Also electron is at rest at the beginning and it is called a recoil electron after the collision.

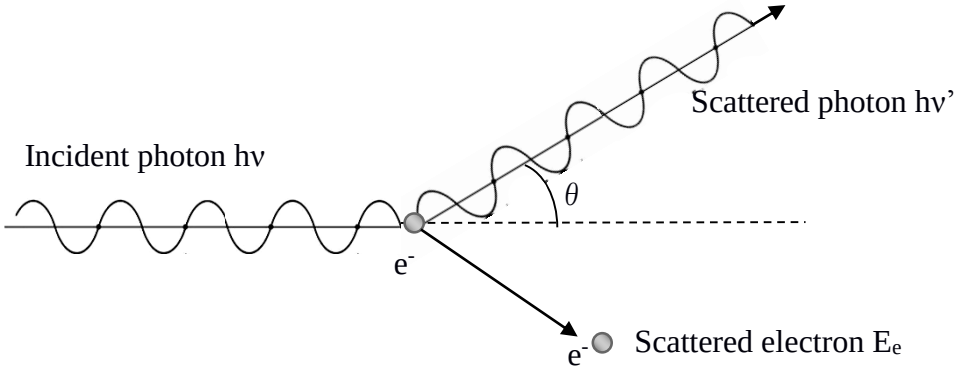


Figure 4.3: The schematic view of Compton scattering.

By writing the equations for conservation of momentum and energy, the scattered gamma-ray energy simply can be found. In equation 4.2 same symbols used with Fig. 4.3 and $m_0$ is a rest mass of the initial electron.

$$h\nu' = \frac{h\nu}{1+\frac{h\nu}{m_0c^2}(1-\cos\theta)}$$

$$E_{e^-} = h\nu - h\nu' = h\nu\left(\frac{\left(h\nu/m_0c^2\right)\left(1-\cos\theta\right)}{1+\left(h\nu/m_0c^2\right)\left(1-\cos\theta\right)}\right) \qquad (4.2)$$

The probability of Compton scattering depends on the number of electrons in the absorber atom. While with equation 4.3 the energies of scattered photon and electron are computed, this equation does not say anything about the probabilities of finding a scattering photon at one angle relative to another. However Klein-Nishina formula predicts the angular distribution of scattered gamma-ray for the differential scattering cross-section

$$\frac{d\sigma}{d\Omega} = Zr_0^2\left(\frac{1}{1+\alpha\left(1-\cos\theta\right)}\right)^2\left(\frac{1+\cos^2\theta}{2}\right)\left(1+\frac{\alpha^2\left(1-\cos\theta\right)^2}{\left(1+\cos^2\theta\right)\left[1+\alpha\left(1-\cos\theta\right)\right]}\right), \qquad (4.3)$$

where $r_0$ is the classical electron radius. The distribution is shown graphically in Fig. 4.4 (a), where the strong tendency of forward scattering for high energy gamma-ray can be seen. Fig. 4.4 (b) shows the shape of the distribution of Compton recoil electrons, $E_C$ is the gap between maximum Compton recoil electron energy and the incident gamma-ray energy.

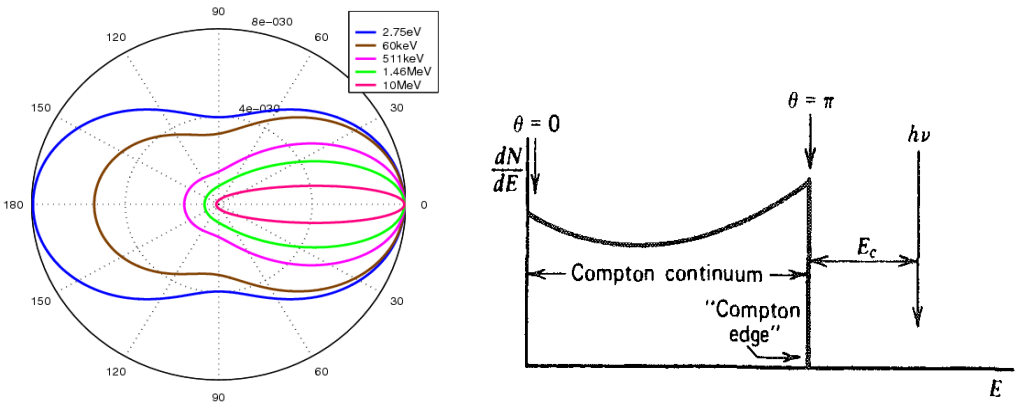


(a) (b)

Figure 4.4: (a) The results for Klein-Nishina formula results the scattering angle probabilities change with respect to energy of the γ rays.[22].(b)distribution of Compton recoil electron. [22]

Compton scattering can take place when the initial electron is free or unbounded. In actual detectors, however, electrons have a binding energies. This makes an effect on the shape of the Compton continuum. This effect is mostly seen for the low energetic gamma-rays and the Compton edge becomes smoother.

### 4.1.3 Pair Production

Another mechanism for gamma-ray interaction with matter is pair production. The process occurs near the nuclei in the intense electric field area, where the photon totally disappears and an electron- positron pair is created. For pair production to happen, the gamma-ray energy must be more than 1.022 MeV, which is equal to two rest mass of the electron or positron (0.511 MeV). The excess energy is shared between positron or electron. The schematic diagram is shown in figure 4.5. When $E_{e-}$ and $E_{e+}$ are the kinetic energies of electron ($e^-$) and positron ($e^+$), $h\nu$ is gamma-ray energy and $m_0c^2$ is the rest energy of electron or positron, the relation between them is $E_{e^-} + E_{e^+} = h\nu - 2m_0c^2$ . The pair production process can be pictured as shown in Fig. 4.5.

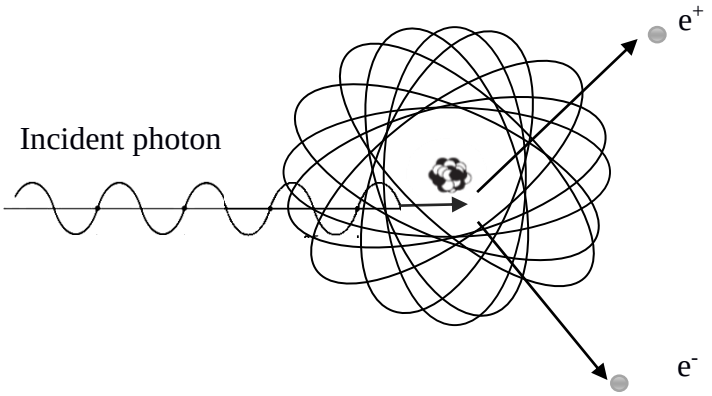


Figure 4.5 A schematic picture for pair production process. The conversion of gamma-ray into the positron and electron.

The probability equation for pair production is not given, however in Fig. 4.1 it's clear that the cross section of pair production increase above 5 MeV. Created positron annihilate or combine with e- in the absorber medium, both of them disappear and as secondary products two photons are created. These two photons have energies of 0.511 MeV each.

### 4.2 γ-Ray Transition and Selection Rules

During a γ-ray transition, energy and momentum are conserved. The initial nucleus with mass M is at rest. To conserve energy, the difference between initial excited state and the final state must be equal to gamma-ray energy and recoil kinetic energy of the nucleus. To conserve linear momentum the initial momentum is zero since the nucleus is assumed to be at rest, consequently, final nucleus should have a recoil momentum which compensate for the momentum of the gamma ray. This is expressed as $E_i - E_f = E_\gamma + T_R$. Here, $T_R$ is the non-relativistic recoil energy which is equal to $p_R^2/2M$ . $E_i$ represents the initial, $E_f$ represents the final level energies and $E_\gamma$ is the γ-ray energy. From the energy conservation equation solution, the gamma-ray energy is calculated as

$$E_\gamma = Mc^2\left[-1 \pm \left(1 + 2\frac{\Delta E}{Mc^2}\right)^{1/2}\right] \tag{4.4}$$

where ΔE is defined as the energy difference between initial and final level. ΔE is in the order of MeV, and $Mc^2$ is in the order of $Ax10^3$ MeV. When the term in the square root is expanded, the second part is in the order of $10^{-4}$.Therefore the recoil correction $(\Delta E)^2/Mc^2$ to the gamma-

ray energy is generally negligible, so $E_\gamma$ can be taken to be equal to $\Delta E$.

The classification of γ-ray radiation by its multipolarity and parity is connected to its electromagnetic properties and on the properties of the initial and final nuclear states. The spin (I) and parity (π) is the main properties of states. The emission of a γ ray is same process with the creation of electromagnetic wave so it should obey the Maxwell equations. The distribution of charge and current in the nucleus creates the electric $\vec{E}(\vec{r},t)$ and magnetic $\vec{B}(\vec{r},t)$ field. These fields transfer both energy and angular momentum. A detailed explanation of γ-ray radiation can be found in ref.s [23]. In the γ-ray decay process, photon is the only particle emitted and it has an integer intrinsic spin. The angular momentum of the photon, L, is called the multipole order of radiation. The angular momentum L and parity π carried by the photon are determined by the conservation law.

$$\vec{I}_f = \vec{L} + \vec{I}_i$$

$$\pi_i \times \pi = \pi_f$$

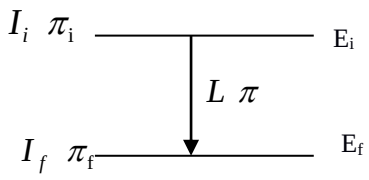


Figure 4.6: Basic representation of γ-ray transition between initial and final states.

Since $\vec{I}_i$, $\vec{I}_f$ and $\vec{L}$ must form a closed vector triangle. The possible values of L are restricted with $|I_i - I_f| < L < I_i + I_f$. The type of radiation (electric or magnetic) depends on the parity of initial and final level. If parity doesn't change then the radiation field has an even parity, if parity changes then the radiation field have an odd parity. Therefore electric and magnetic multipoles differ in their parities. If radiation field have an odd parity, even electric multipoles and odd magnetic multipoles transitions are formed. The transitions can also have mixed multipolarities.

Finally the gamma-ray transition selection rules for angular momentum and parity are given as:

- multipolarity order of γ rays is decided with $|I_i - I_f| < L < I_i + I_f$ equation. If the initial and final spin values for states are same, then the only value for L is zero. But L=0 is forbidden transition, since photon has to carry angular momentum.
- Multipolarity of γ rays is decided with respect to change of parities between initial and final state;
    - If there is no parity change ($+ \rightarrow +$, $- \rightarrow -$) then the characteristic of γ rays can be even electric or odd magnetic.
    - If there is a parity change ($+ \rightarrow -$) then the characteristic of γ ray can be odd electric or even magnetic.

The exception to the selection rules happens when initial and final angular momentums are equal, because there is no monopole transition. For this situation the minimum multipole order is 1. Other situation is, if the initial or the final level has a zero angular momentum, then the transition is pure multipole, comes from above selection rules. And if both of the states has 0 angular momentum then selection rules gives only the L=0 but it's not permitted. These states decay by internal conversion. In this process, the extra energy is emitted by throwing out an electron, this electron is mostly ejected from the K shell of the atom. Also internal conversion cross section is increased with increasing atom number or nuclear radius.

One other important point is to calculate the probabilities of which multipole transitions are more probable. As mentioned before, for one transition there are several permitted multipole transitions. There are two approaches to find these values. One of them is single particle estimation that based on shell model, which assumes one nucleon excitation contribute to the radiation. The other is collective aspect that based on liquid drop model, which the radiation created from several nucleons excitation. The single particle estimate (Weisskopf) to find transition probabilities per unit time are explained in Krane [18].

The decay probability per unit time for a photon with energy ħω is given by

$$\lambda(\sigma L) = \frac{P(\sigma L)}{\hbar\omega} \tag{4.7}$$

The symbol σ represents the electric or magnetic transition, it can be E or M and P(σL) is radiation power which depends on amplitude of the electric or magnetic multipole moment m(σL). The radiation power P(σL) and matrix element of multiple operator that change nucleus from initial state to final state are given as [18]:

$$P(\sigma L) = \frac{2(L+1)\,\mathrm{e}}{\varepsilon_0 L\left[(2L+1)!!\right]^2}\left(\frac{\omega}{c}\right)^{2L+2}\left[m(\sigma L)\right]^2 \ , \tag{4.8}$$

$$m_{fi}(\sigma L) = \int \psi_f^{*}\, m(\sigma L)\, \psi_i dv. \tag{4.9}$$

Then the final form of decay probability found is substituting equation 4.8 into equation 4.7:

$$\lambda(\sigma L) = \frac{2(L+1)}{\varepsilon_0 \hbar L\left[(2L+1)!!\right]^2}\left(\frac{\omega}{c}\right)^{2L+1}\left[m_{fi}(\sigma L)\right]^2. \tag{4.10}$$

It is found that, with some approximations, the final transition probabilities can be expressed in such a way that they only depend on the γ-ray energy, angular momentum and the mass number of nucleus.

Table 4.1: Weisskopf estimate results from ref. [18]. E's are given in MeV and λ in $s^{-1}$.

| **σL** | **λ(σL)** |
|---|---|
| E1 | $1.02 \times 10^{14} A^{2/3} E^{3}$ |
| E2 | $7.23 \times 10^{7} A^{4/3} E^{5}$ |
| E3 | $3.37 \times 10 A^{2} E^{7}$ |
| E4 | $1.06 \times 10^{-5} A^{8/3} E^{9}$ |
| E5 | $2.38 \times 10^{-10} A^{10/3} E^{11}$ |
| M1 | $3.13 \times 10^{13} E^{3}$ |
| M2 | $2.21 \times 10^{7} A^{2/3} E^{5}$ |
| M3 | $1.03 \times 10 A^{4/3} E^{7}$ |
| M4 | $3.25 \times 10^{-6} A^{2} E^{9}$ |
| M5 | $7.29 \times 10^{-13} A^{8/3} E^{11}$ |

Although theoretical Weisskopf estimate give us an idea of the transition probabilities, they cannot be directly compared to the measured values. They are good for relative comparisons.

General expectations can be derived from the above formulas and single particle estimation are listed below.

- The lowest permitted multipole usually dominates, such as permitted transition E2 is more probable than E4 and M1 is also more probable than M3.
- Electric multipole transition is more probable than the magnetic multipole transition. For example the transition probability of E1 is 10 times higher than M1 and $10^{7}$ times higher than M2.
- Emission of multipole order L+1 less probable than emission of multipole order L by a factor of the order of about $10^{-5}$ ,as an example E3 and E4 or M3 and M4 also in different type of transitions M1 and E2.

### 4.3 Angular Distribution and Polarization of Photons

Angular distribution and polarization of γ rays emitted from an excited nucleus provides valuable information about multipolarity and the nature (E or M) of the γ ray. Knowing these and the properties (spin, parity) of a ref. state, e.g. ground state, one can determine the spin and parity of an excited state in a level scheme.

Assuming there is no mixing of different multipolarities, the angular distribution at the lowest order can be written as [24]

$$W(\theta) = 1 + \alpha_2 A_2 P_2(\cos\theta) + \alpha_4 A_4 P_4(\cos\theta)$$
$$or \qquad (4.11)$$
$$W(\theta) = \sum a_x P_x(\cos\theta),$$

where $A_2$ and $A_4$ are angular distribution coefficients and $\alpha_2$ and $\alpha_4$ are attenuation coefficients for fully aligned or partially aligned states. Here, $a_x = \alpha_x A_x$ and it is a Legendre coefficient. $P_2(\cos\theta)$ and $P_4(\cos\theta)$ are Legendre polynomials. The attenuation and Legendre coefficients for aligned and partially aligned nuclei are calculated and tabulated by Yamazaki and Matesian [24] for different initial and final states.

A nuclear state with spin I has 2I+1 sub states with m=-I, (-I+1),…, (l-1),+l and there are $(2I_i+1)$ x $(2I_f+1)$ transitions between the initial and the final levels. In an external magnetic field the energies of this sub states would split up as it is shown in Fig. 4.7(b). This changes the energies of the transitions but the splitting is typically so small that one cannot resolve the different transition energies. One can only measure a mixture of all possible transitions.

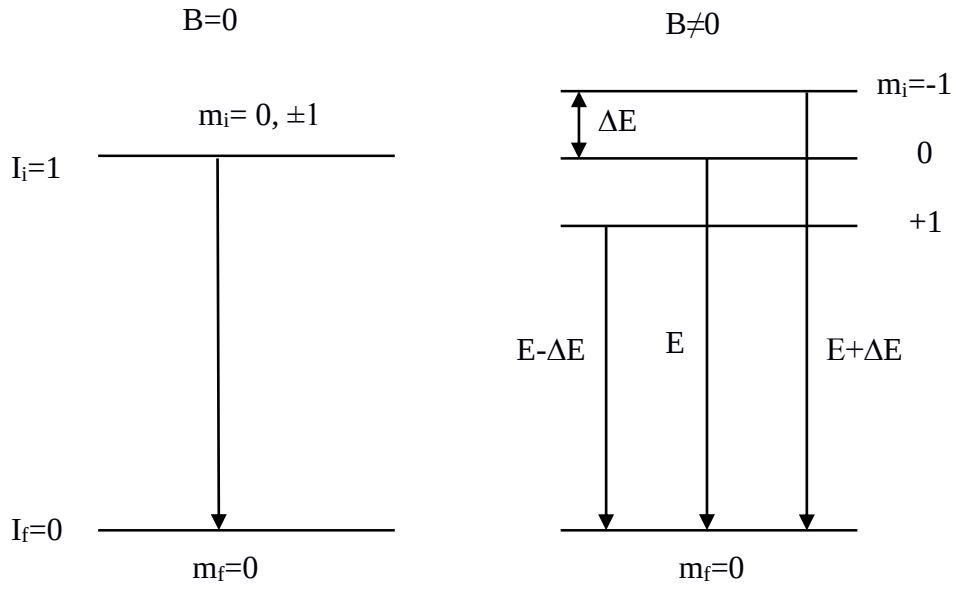


Figure 4.7: The schematic representation of γ-ray transitions with sub-states.

It is also possible to express the angular distribution function W(θ) as a function of population of different m sub-states.

$$W(\theta) = \sum_{m_i} p(m_i) W_{m_i \to m_f}(\theta) \tag{4.12}$$

where the $p(m_i)$ is the population of the state $m_i$. Under normal circumstances, the nuclear states are non-oriented and the populations of the sub states are equal to p(m)=1/(2I+1) for all m values. However, after heavy ion reactions, the nucleus is oriented due to the large angular momentum transfer. The oriented states are classified as:

if P (m) = P (-m) → there is alignment,

if P (m) ≠ P (-m) → the population is polarized,

if a state is completely aligned,

$$P(m) = \begin{cases} 1 & \text{for m} = 0 \\ 0 & \text{otherwise} \end{cases}.$$

The sub state population can be described as a Gaussian distribution with a half width of σ centered on m=0. If the nuclei have a perfect alignment, σ/I is close to zero. For heavy-ion fusion reactions σ/I value is fairly constant around 0.3-0.4.

### 4.3.2 DCO Ratio Method

The directional correlations of γ rays de-exciting oriented states (DCO ratio method) is used widely in order to determine the multi polarities of γ-ray transitions. The angular correlation of γ-rays from oriented state depends on the populations of the m sub states.

In this method, two consecutive γ rays are emitted at angles $\theta_1$ and $\theta_2$ with respect to the beam axis (z-axis) shown in Fig. 4.2. And the $\Delta\varphi=\varphi_1-\varphi_2$ is the angle between the planes defined by the z-axis and the outgoing γ-rays in Fig. 4.8.

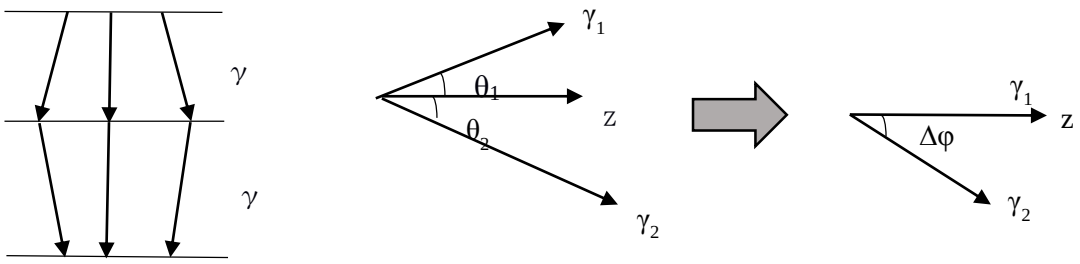

Figure 4.8: A schematic representation of two coincident γ rays and the correlation angles with respect to beam axis, z axis.

The angular correlation function is W ($\theta_1$, $\theta_2$, $\Delta\varphi$) is a modified version of equation 4.9 [25] and the DCO ratio is defined as

$$R_{DCO} = \frac{W(\theta_1, \theta_2, \Delta\varphi)}{W(\theta_2, \theta_1, \Delta\varphi)} \quad . \tag{4.13}$$

The experimental DCO ratio is obtained from the intensities in an $E_\gamma$-$E_\gamma$ matrix in the following form:

$$R_{DCO} = \frac{I(\gamma_1 \text{ at } \theta_1, \text{gated with } \gamma_2 \text{ at } \theta_2)}{I(\gamma_1 \text{ at } \theta_2, \text{gated with } \gamma_2 \text{ at } \theta_1)}. \tag{4.14}$$

Theoretically calculated values from equation 4.13 can be compared to the experimental values and the multipolarity of the γ-ray transition can be determined.

### 4.3.3 Linear Polarization

Alongside the angular correlation method which can only determine the multipolarity of a γ-ray transition, the polarization measurement which can differentiate between electric and magnetic nature of transitions is also needed in order to make firm spin and parity assignments. As mentioned before γ-rays from oriented states are polarized. Compton scattering is sensitive to the polarization of the incident γ-ray, the scattering cross-section being larger in the direction normal to the electric vector. Polarization correlation function is shown as W (θ, γ), where the γ is the angle between the reaction plane and the electric vector of emitted γ-ray, as given in Twin's article [25].

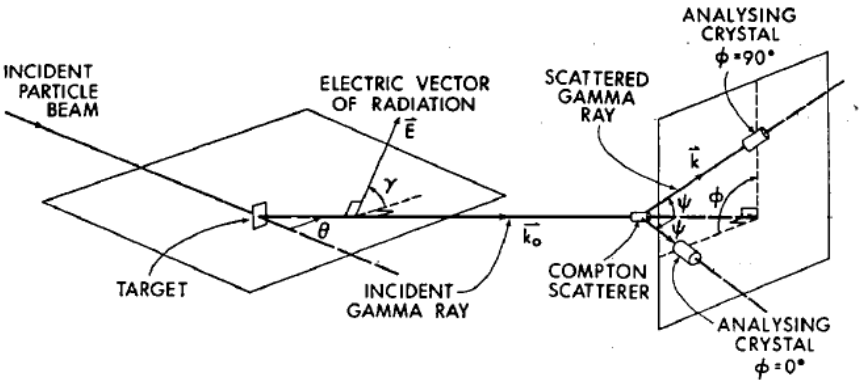


Figure 4.9: A schematic view of Compton scattered γ-rays and a detector system. Taken from Twin [25].

The theoretical polarization is given as

$$p_t = \frac{W(\theta,\gamma=0^o) - W(\theta,\gamma=90^o)}{W(\theta,\gamma=0^o) + W(\theta,\gamma=90^o)}, \tag{4.15}$$

where $p_t$ values are between +1 and -1 and $p_t$=0 showing the unpolarized γ ray. Experimental polarization is determined by

$$P = \frac{1}{R}\frac{N(\theta,\varphi=0) - N(\theta,\varphi=90)}{N(\theta,\varphi=0) + N(\theta,\varphi=90)}, \tag{4.16}$$

where N (θ, φ=90°) is the photon intensity of vertically scattered γ rays and N (θ, φ=0°) is the intensity of horizontally scattered γ-rays. The scattering plane is determined by the beam direction and the direction of the emitted γ ray. The polarization efficiency R of the polarimeter is given by

$$R = \frac{\sin^2\psi}{k_0/k + k/k_0 - \sin^2\psi}, \tag{4.16}$$

and it can be determined by making use of the Compton scattering Klein-Nishina formula. Here, k and $k_0$ are the wave numbers of the incoming and scattering radiation and ψ angle is shown in Fig. 4.9.

For only dipole and quadrupole transitions, theoretical polarization at θ=90° takes the following forms [25] :

Dipole: $$p_t = \pm\frac{3a_2}{2-a_2} \quad \begin{Bmatrix} +\text{magnetic} \\ -\text{electric} \end{Bmatrix},$$

Quadrupole: $p_t = \pm \dfrac{3a_2 + 1.25a_4}{2 - a_2 + 0.75a_4} \quad \left\{ \begin{matrix} + \text{electric} \\ - \text{magnetic} \end{matrix} \right\}.$

These $a_2$ and $a_4$ coefficients are explained before in angular correlation part as Legendre coefficients. By using these theoretical formulas, one can calculate polarization of a γ ray and compare the theoretical values with the experimental results.

# CHAPTER 5

# EXPERIMENTAL RESULTS

In this chapter, the experimental results will be explained under two major and three minor headings. First the γ-ray transitions of $^{91}$Ru nucleus is explained with the minor topic of the new transitions belonging to this nucleus. Secondly the spin and parity assignments of γ-ray transitions will be mentioned in two minor headings with Asymmetry and $R_{DCO}$.

## 5.1 γ-ray Transitions in $^{91}$Ru

During the experiment the compound nucleus $^{94}$Pd was formed by a heavy-ion fusion-evaporation reaction in a process which was explained in part 2.1. The $^{58}$Ni target with an average thickness of 6 mg/cm$^3$ was used which was isotropically enriched to 99.8 %, bombarded by $^{36}$Ar beam, which had an energy of 111 MeV and an average intensity of 10pnA. The reaction was:

$$^{36}_{18}Ar + ^{58}_{28}Ni \rightarrow ^{94}_{46}Pd^{*}.$$

The compound nucleus $^{94}$Pd first emits charged particles e.g. protons, α particles and neutrons. This emission process continues until there is not enough energy to remove particles. Then the residual nuclei emit γ rays until they reach their ground states. Table 1 show the daughter nuclei which were populated with highest cross-section.

Table 5.1: Daughter nuclei, populated after $^{36}_{18}Ar + ^{58}_{28}Ni \rightarrow ^{94}_{46}Pd^{*}$ reaction. Four reaction channels are highlighted to draw attention to highest cross-sections at the given beam energy.

| $^{94}_{46}Pd*$ | n=0 | n=1 | n=2 | n=3 |
|---|---|---|---|---|
| p=0 | $^{94}_{46}Pd*$ | $^{93}_{46}Pd$ | $^{92}_{46}Pd$ | $^{91}_{46}Pd$ |
| p=1 | $^{93}_{45}Rh$ | $^{92}_{45}Rh$ | $^{91}_{45}Rh$ | |
| p=2 | $^{92}_{44}Ru$ | $^{91}_{44}Ru$ | $^{90}_{44}Ru$ | |
| p=3 | $^{91}_{43}Tc$ | $^{90}_{43}Tc$ | | |

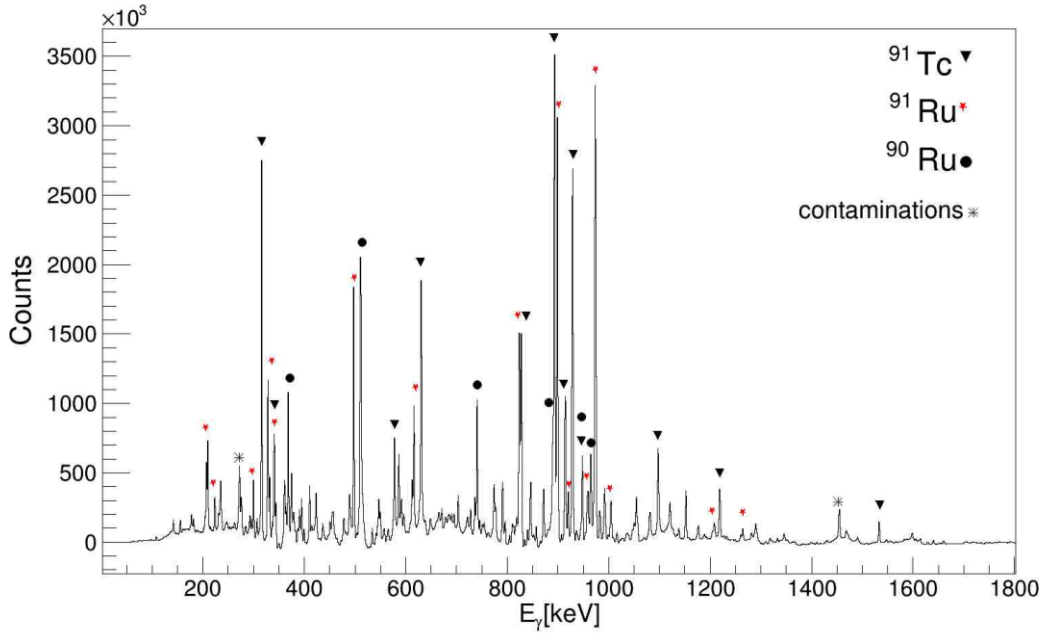


Figure 5.1- The spectrum shows the total projection of the γ - γ energy matrix. The γ- ray transitions from the most dominant reaction channels are marked on the figure.

As one can see from table 1 the dominant decay mode is three nucleon emission and the corresponding nuclei are $^{91}$Ru, $^{91}$Tc, $^{91}$Rh and $^{91}$Pd. As mentioned in sect. 2, in the ancillary detector part, the efficiency of the neutron detectors is not perfect and it decreases when the number of detected neutron increases. Therefore, 3n ( ${}^{91}_{46}Pd$ ) and 2n ( ${}^{91}_{45}Rh$ ) channels are less visible in the γ- ray spectrum as compared to 1n ( ${}^{91}_{44}Ru$ ) and 0n ( ${}^{91}_{43}Tc$ ) channels. The γ-ray transitions from the three dominant reaction channels, 3p channel leading to ($^{91}$Tc), 1n2p channel leading to ($^{91}$Ru), and 2n2p channel leading to ($^{90}$Ru) are marked in fig. 5.1.

For analyzing the $^{91}$Ru nuclei, new $E_\gamma$-$E_\gamma$ matrix is constructed with the condition of 1n and 2p. Total number of events in 1n2p condition is 3x $10^7$. The Radware package [14] specifically gf3 and escl8rt programs were used to analyze the data. The total projection of the 1n2p gated γ-γ energy matrix is shown in Fig. 5.2. (a) In this spectrum most of the γ-ray transitions belongs to $^{91}$Ru.

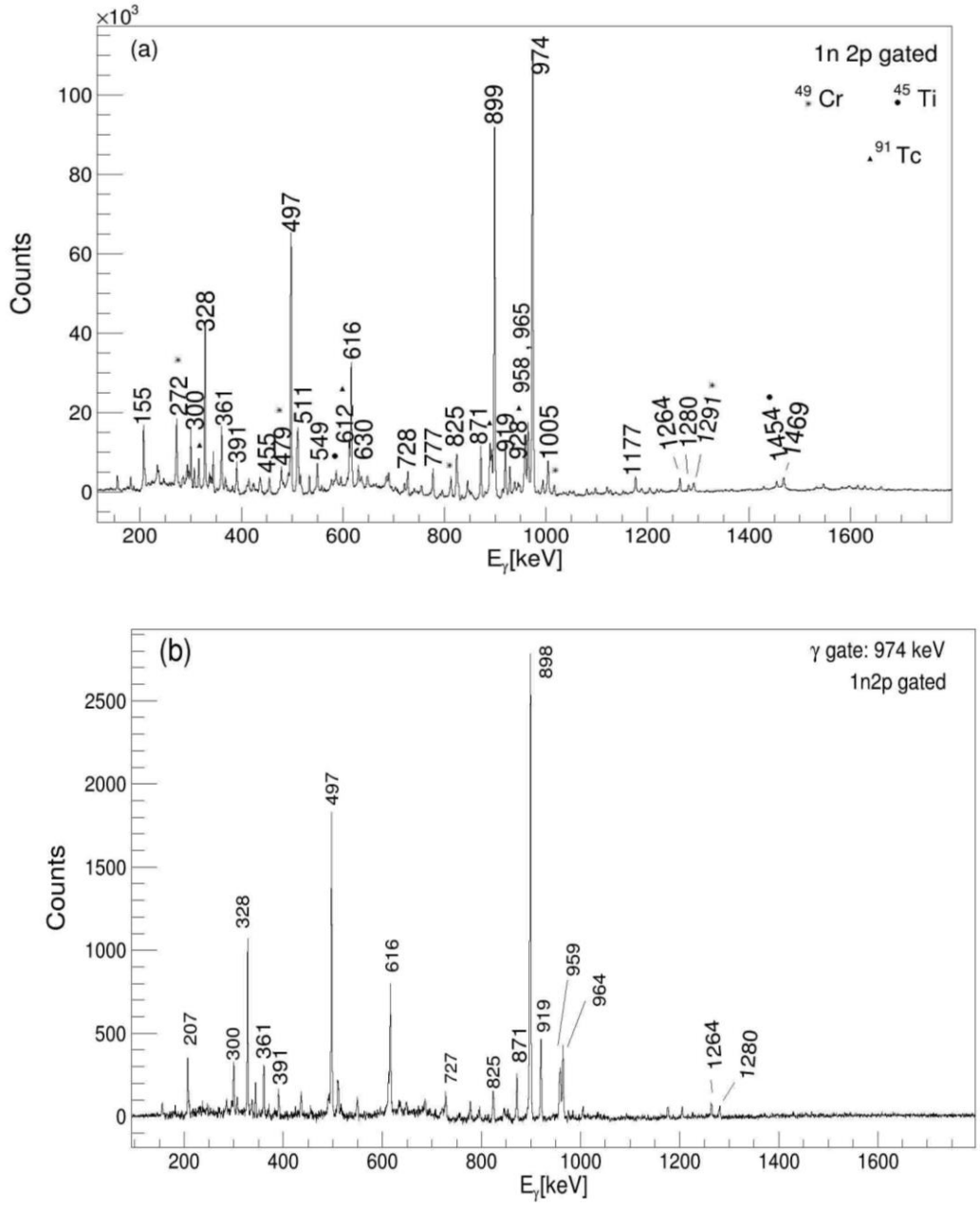


Figure 5.2: (a) The spectrum shows the total projection of γ - γ matrix sorted with a condition of 2 detected protons and 1 detected neutron. The energies of the known transitions in $^{91}$Ru are written on the figure. The symbols * and ▲ represent the contaminations from $^{49}$Cr and $^{45}$Ti, respectively and the $^{91}$Tc (3p) leak to 2p1n channel is marked with ●. (b) Gamma ray gated energy spectrum obtained by gating on the 974 keV transition in 91Ru. Both of the spectra are Compton background subtracted.

Although the spectrum shown in Fig. 5.2 (a) is 1n2p gated, there are some contaminations which are marked on the figure. Since the vacuum in the beam and in the target target chamber is not ideal, contaminations which come from the other reactions can also be seen. For

example, $^{49}$Cr nucleus is created when the beam reacts with $^{16}$O:

$$^{36}\mathrm{Ar} + ^{16}\mathrm{O} \rightarrow {}^{49}\mathrm{Cr} + 2\mathrm{p}1\mathrm{n}.$$

Also, $^{45}$Ti and $^{46}$Ti are formed when the beam react with $^{12}$C in the target:

$$^{36}\mathrm{Ar} + ^{12}\mathrm{C} \rightarrow {}^{45}\mathrm{Ti} + 2\mathrm{p}1\mathrm{n}$$
$$^{36}\mathrm{Ar} + ^{12}\mathrm{C} \rightarrow {}^{46}\mathrm{Ti} + 2\mathrm{p}.$$

Gamma-ray transitions from the target like $^{58}$Ni and $^{59}$Ni nuclei are also observed in the different gated spectra. $^{91}$Tc is one of the most strongly populated nucleus, and the transitions from this nucleus can clearly be seen in Fig. 5.2 marked by ▲.

To reduce the contributions from other reaction channels, one can take advantage of the γ- ray coincidence method. With this method, one can select the cascade of γ-rays which are coincidence with the selected γ ray energy. A gate was set on the lowest transition of $^{91}$Ru ($E_\gamma$ =974 keV, $13/2^+ \rightarrow 9/2^{+)}$ in the 1n2p γ-γ matrix, and the spectrum was cleaned from other reaction channels and contaminations, Fig. 5.2 (b).

### 5.1.1 Newly observed transitions

The level scheme of $^{91}$Ru nucleus was studied before by Arnell and Hesse [6, 7], so most of the γ-ray transitions in figure 5.2(b) are known. Apart from the known γ-ray transitions, 6 new transitions were observed in this work. Among the new transitions 1280 keV, 520 keV, 686 keV and 234 keV lines are in coincidence with the lowest lying 974 keV transition and subsequent of 974 keV.

In Fig. 5.3(a) the 234 keV gated spectrum shows the coincidence γ-ray transitions with 234 keV γ-ray transition. From this spectrum one can easily see that the 361 keV transition cross section is bigger than the others. This can mean that 234 keV transition follows the 361 keV transition in the level scheme. In addition to known transitions from ref. [6, 7] 686 keV, 1614 keV and 1660 keV transitions can be seen as a newly observed transition. Also 740 keV γ-ray is seen in 234 keV gated spectrum, however this transition does not belong to $^{91}$Ru nucleus, because it has no coincidence with known or newly observed transition except 234 keV. And 740 keV transition was observed before in $^{88}$Mo nucleus and $^{69}$Ge nucleus [26, 27] as a coincidence with 234 keV transition.

In Fig. 5.3 (b) the 520 keV gated spectrum shows the coincidence γ-ray transitions with 520 keV transition. As a difference from Fig. 5.3 (a), 520 keV transition doesn't have the coincidence with 361 keV and 300 keV, also 520 keV gated spectrum does not have a peak in 234 keV energy which means that 234 keV and 520 keV transitions probably parallel to each other. As a similarity with 234 keV both have a connection with 1660 keV and 1614 keV transitions.

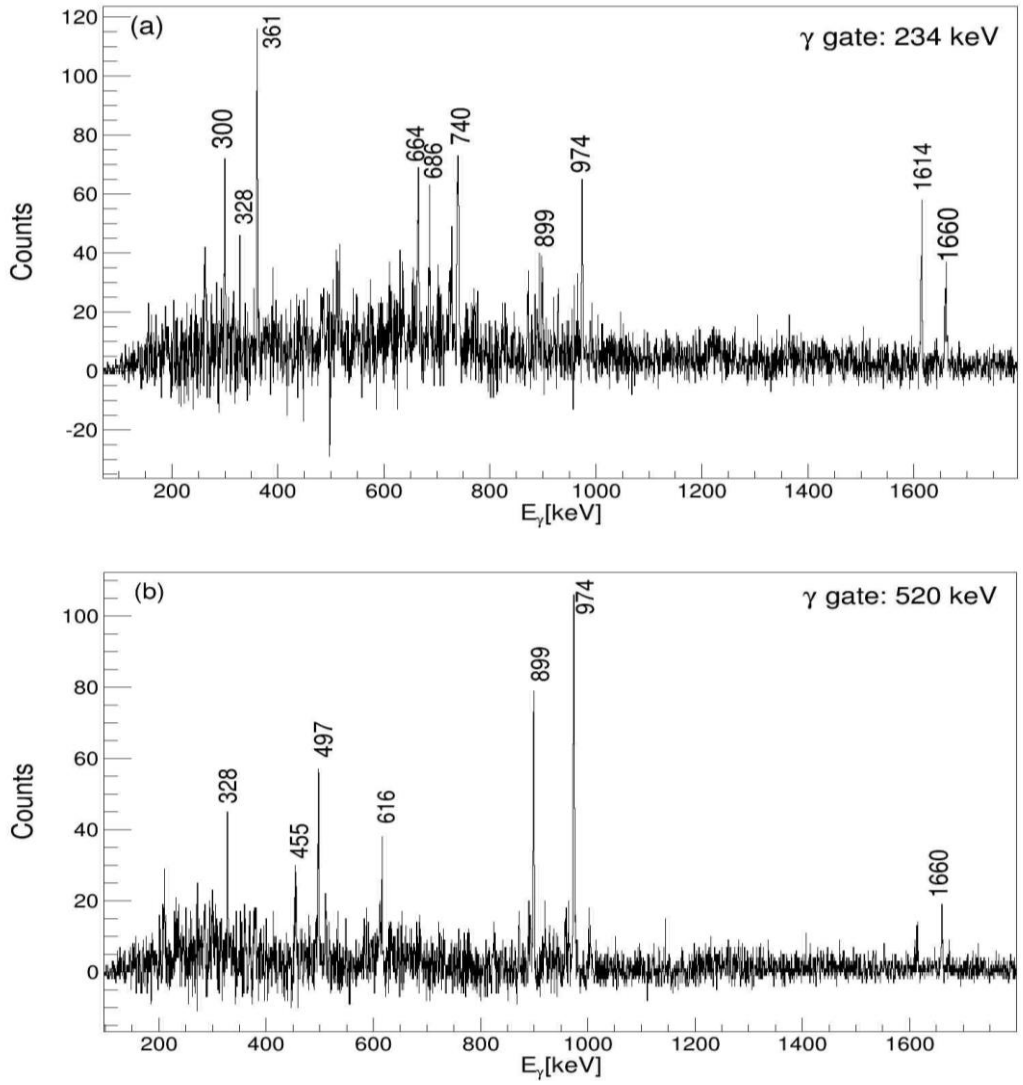


Figure 5.3: (a) 234 keV gated, (b) 520keV gated spectrums. And backgrounds are subtracted from γ -ray spectra.

In Fig. 5.4(a) 686 keV coincident γ-rays are shown. For the Fig., 686 keV transition has a coincidence with 234 keV transition and 974 keV transition. 686 keV transition is also has an coincidence with 307 and 209 keV transitions which means that as an energetically 686 keV transition can be connection between 1660 keV and 974 keV states.

Fig. 5.4 (b) shows the coincidence γ-rays with 1280 keV transition. As can be seen from figure 1280 keV gated spectrum is cleaner than the other newly observed ones. And it just shows four clear peaks at 974 keV, 155 keV, 272 keV and 300 keV. 272 keV transition is also seen in Fig. 5.2(a) as a contamination from $^{49}$Cr nucleus.

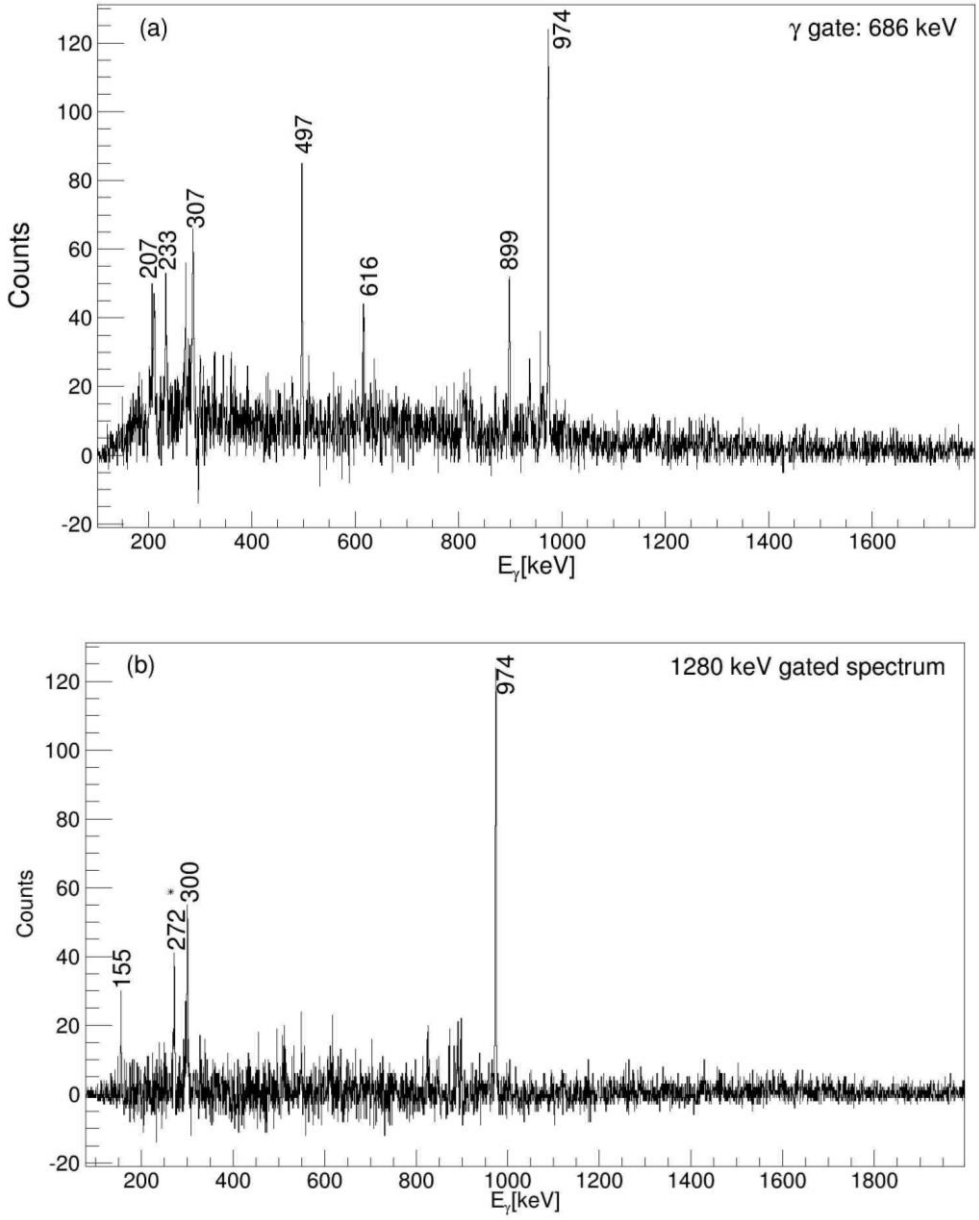


Figure 5.4 (a) 686 keV gated γ-ray spectrum (b) 1280 keV gated γ-ray spectrum. Both spectra are background subtracted. The 272 keV contamination line from $^{49}$Cr is marked with * in the spectrum.

In addition to these new transitions, that are coincidence with 974 keV, there are also two other transitions which can be placed parallel to the 974 keV transition. These are 1660 keV and 1614 keV transitions. It is also possible that a 46 keV transition connects the 46 keV state to the ground state. However, 46 keV transition cannot be observed because of internal conversion or low detector efficiency at the low energies. Internal conversion is an electromagnetic process in which nuclei give the excess energy to the inner shell (K shell) electron instead of releasing a γ ray. The probability of internal conversion increases as the γ-

ray energy decreases [18].

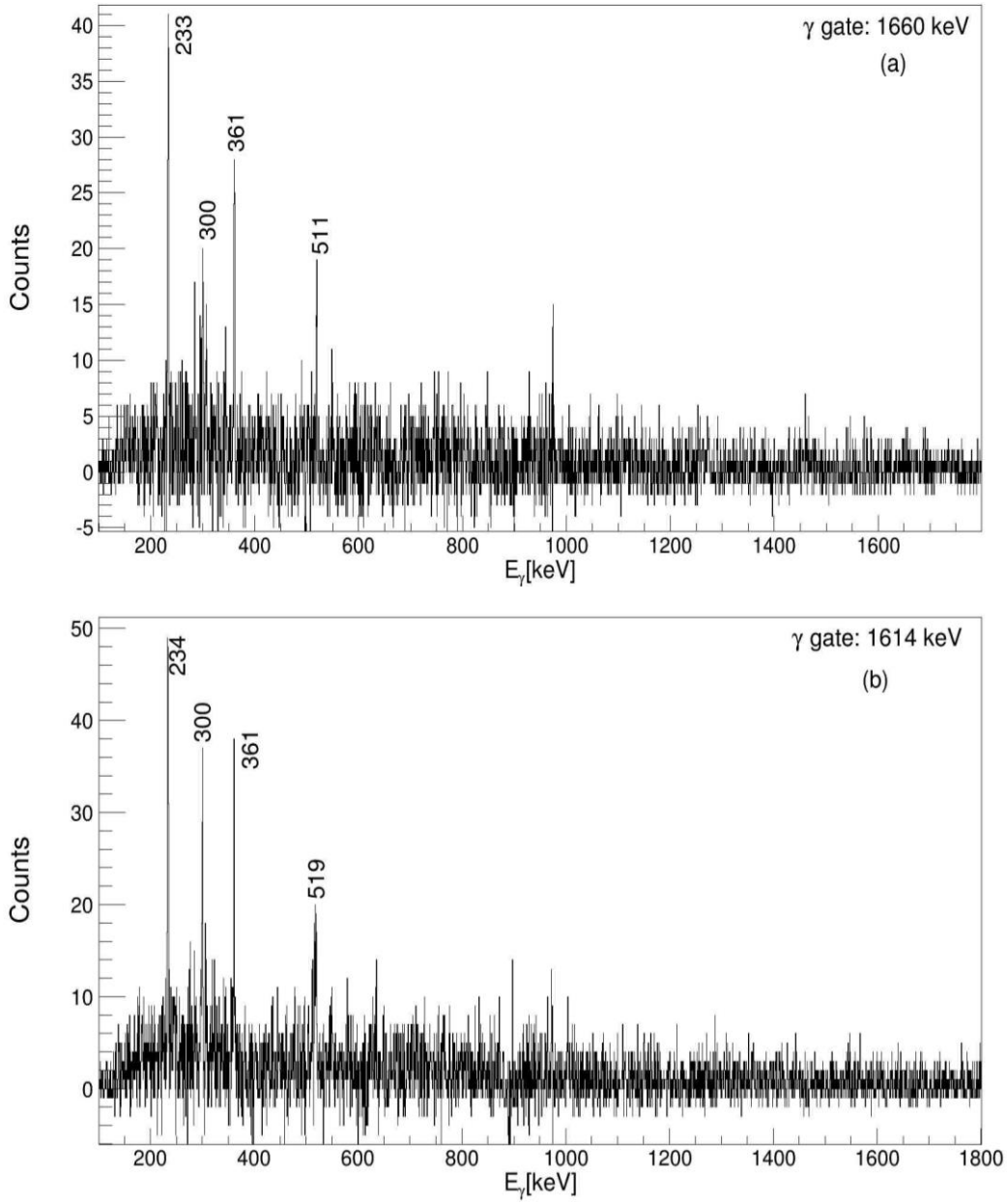


Figure 5.5:1660 keV and 1614 keV gated spectra, background is subtracted.

From the γ-ray coincidences seen in Fig.: 5.3, 5.4and 5.5, it was possible to place the newly observed γ rays in the level scheme of $^{91}$Ru. For example in 1280 keV gated spectrum in Fig.5.3(c), shows three clear transitions at 155 keV, 300 keV and 974 keV. From these coincidences, and the intensities of transitions one can say that 1280 keV transition probably is in between 2709 keV state and ground state. Although there are several possible places to locate 1280 keV transition, the unseen transitions which belong to 2709 to 0 keV state region,

gives a clue that this unseen ones must be parallel to1280 keV transition and they are not coincident. Thus, 1280 keV transition is from 2254 keV to 974 keV. Making this kind of analysis to all newly observed transitions, one can locate the new levels to the level scheme of $^{91}$Ru which is shown in fig. 5.6. New energy levels are also found in this work while placing the new transitions. First of all new levels located with respect to energy of the transition, and coincidences with the known transitions. As one can see from Fig. 5.5(a) 1660 keV transition is coincidence with 234 and 361 keV transitions, and the important point is ground state transition is not seen in the spectrum, which means that 1660 keV should be parallel to 974 keV transition. And with looking known transition spectrums such as 361 keV spectrum, one can crosscheck that 1660 keV has a coincidence with 361 keV and 234 keV. With this knowledge first the energy of new level is decided. These new transitions, 234, 686, 1280, 520, 1660, 1614 keV which are reported in this thesis and 12 others were observed independently by Zheng and the updated level scheme was given in the publication [8].

Although the place of new transitions in the level scheme can be found by the energies of γ ray transitions other important point is to find spin and parities of these new levels.

## 5.2 Spin and Parity Assignments

Spins and parities of the nuclear states can be determined by studying the electromagnetic properties of the γ ray transitions. In this section, the DCO Ratio Method and the linear polarization of the γ rays are studied in order to make experimental spin and parity assignments to the newly observed states and to confirm the previously known values.

### 5.2.1 $R_{DCO}$ values

The directional correlation of oriented state method aims to find the multipolarity of gamma rays. With deciding the multipolarity value one can find the spin value of levels. The theoretical explanation of $R_{DCO}$ are given in part 4.3.1, and the experimental formula for $R_{DCO}$ values explained as:

$$R_{DCO} = \frac{\mathrm{I}_{\gamma_1} \text{ at } \theta_1, \text{ gated by } \gamma_2 \text{ at } \theta_2}{\mathrm{I}_{\gamma_1} \text{ at } \theta_2, \text{ gated by } \gamma_2 \text{ at } \theta_1}. \qquad (5.1)$$

For this EXOGAM experiment, $\theta_1$=135$^o$ and $\theta_2$= 90$^o$ since the EXOGAM Ge detectors were located in two different angles, seven at 90$^o$ and four at 135$^o$ relative to beam direction. The detection efficiencies at different γ-ray energies have similar values for detectors at 90 and 135. More information about detectors is in part 2.Two new 2p1n gated γ - γ matrices were constructed for this analysis. In the first one, X-axis showed γ ray energies measured by the 90$^o$ detectors, while the Y- axis showed γ-ray energies deposited in the 135$^o$ detectors. In the second matrix, X-axis and Y-axis were reversed. Gamma-ray gates were set on the X-axis for both matrices. Fig. 5.7 shows the 898 keV gated spectra obtained from the first and second

matrix. The ratio between the peak areas (intensities) obtained from the first and the second matrix gives the $R_{DCO}$ values. The results are shown in Table 5.2 for the 6 new transitions as well as for four previously known transitions.

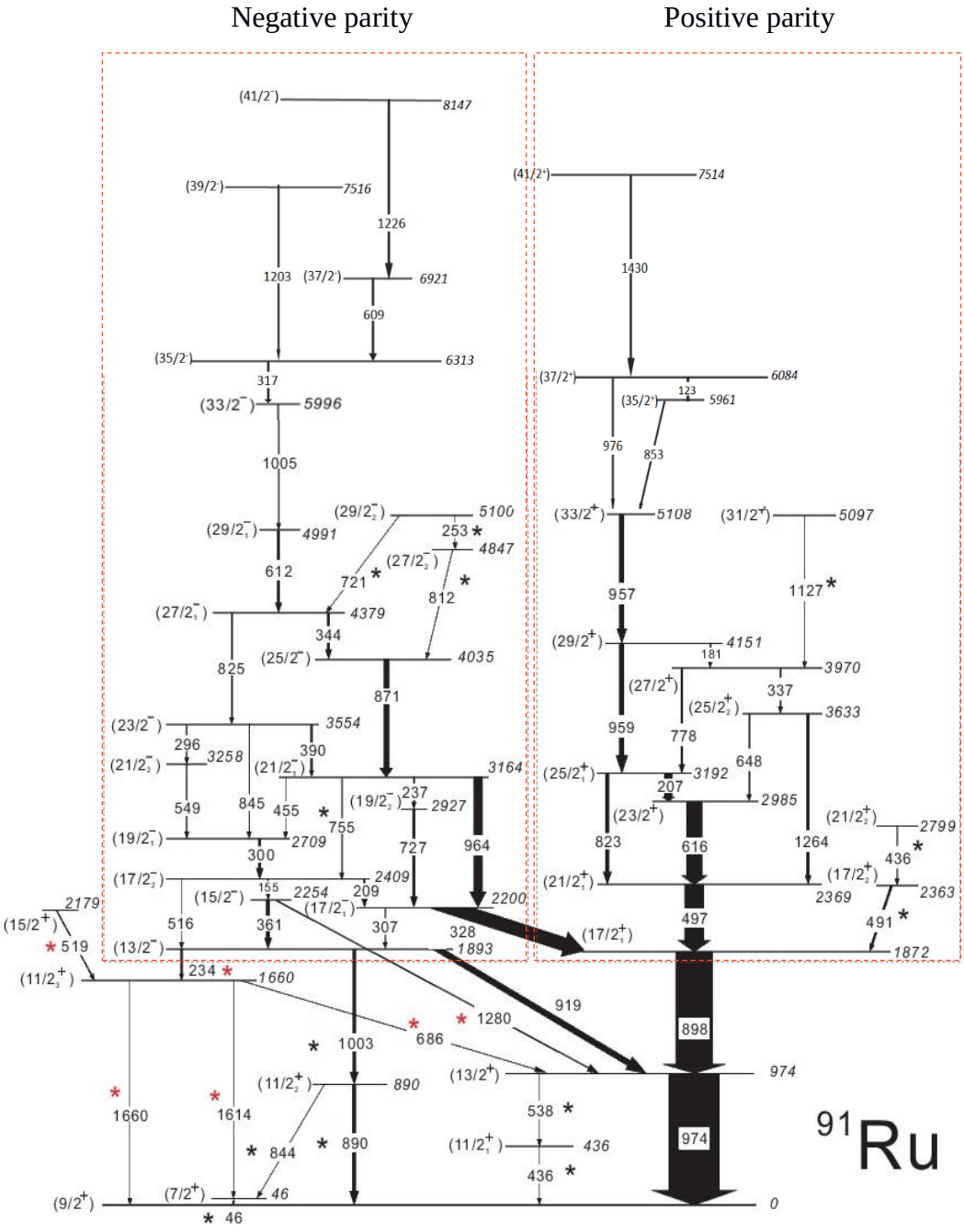


Figure 5.6: Level scheme of $^{91}$Ru. The figure is taken from Zheng et al. [8]. The transitions which were observed in this work are marked with red stars and the transitions observed by Zheng et al. [8] are marked by red and black stars. Rest of the transitions were observed earlier by Arnell and Hesse [6, 7].

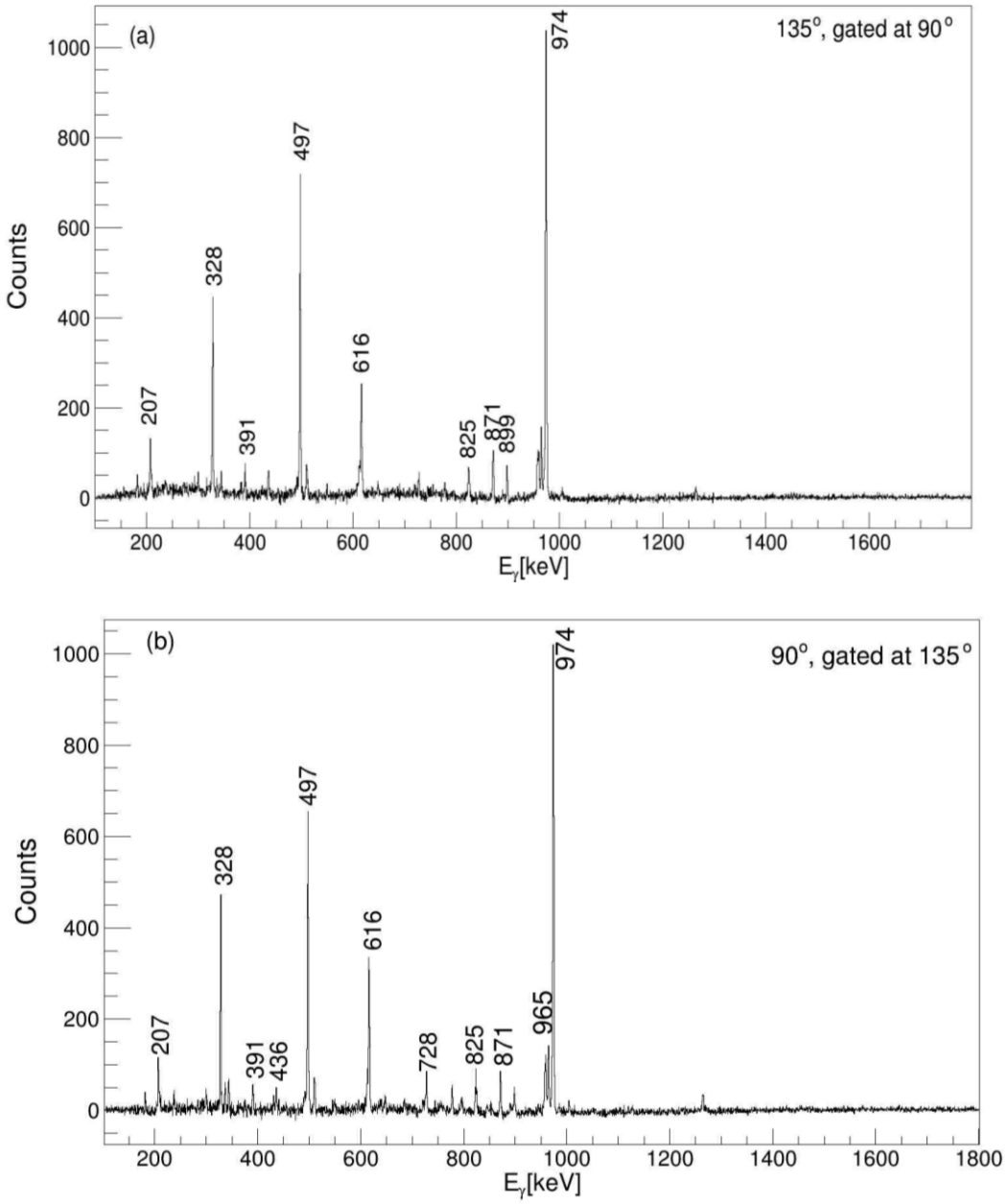


Figure 5.7: 2p1n particle and 899 keV gamma ray energy gated spectra. (a) 135$^o$ detectors gamma energies deposited in y-axis, and 90$^o$ detectors gamma rays stored in x-axis. 899 keV gate is put in the x-axis. (b) x-axis and y-axis are reversed and 899 keV gate is put in the spectrum. both of them background subtracted.

To interpret the RDCO values as a quadrupole or dipole, first the limits and the rules have to be found. The reference values for different type of gates can be fund from theoretical calculations. In this work, this was done by using a DCO code [28] for the EXOGAM geometry. The results showed that, when gated by a stretched quadrupole transition, the

$R_{DCO}$ value for a stretched quadruple transition ($\Delta I = 2$), is ~ 1.0, and for the pure stretched dipole transition ($\Delta I = 1$), is about 0.6 If the gate is put on a pure stretched dipole transition, then the $R_{DCO}$ value for known quadrupole and stretched dipole transitions are ~1.6 and ~1.0 respectively. For a mixed M1+E2 transition, $R_{DCO}$ value varies between 0.6 and 1.0 depending on the multipole mixing ratio of the γ–ray transition. The mixing and mixing ratio is explained in part 3. Furthermore, for non-stretched ($\Delta I = 0$) pure E1 or M1 transitions, the $R_{DCO}$ value is approximately the same as for a stretched quadrupole transition. To get rid of this uncertainty one can need an extra measurements to find characteristics of transitions.

Two low-lying transitions in $^{91}$Ru, namely 898 keV and 974 keV have $R_{DCO}$ close to one in quadrupole gated calculation. These values agree with a stretch quadrupole character, they can be E2 or M2 transition. However previous reports by Arnell and Hesse [7] shows that these two transition are pure E2 transition. So for the interpretation of the $R_{DCO}$ values, we used 898 keV and 974 keV transitions for gates. On the other hand not all transitions has a coincidence with 898 keV and 974 keV transition. Therefore first we found the characteristic and multipolarity of known transitions, then we used this known transitions to find the multipolarity and characteristics of unknown "new" transitions. Table 5.2 shows the intensities and $R_{DCO}$ values of new transitions and also some known transitions. For precise estimations of $R_{DCO}$ values, we also need a polarization measurements.

Table 5.2: Experimental $R_{DCO}$ values, intensities and gates with uncertainties are indicated in table. The new transitions are marked with *.

| $E_\gamma$ (keV) | Gate $_{DCO}$ (keV) | $I_{E\gamma}$ at 90°, gated at 135° | $I_{E\gamma}$ at 135°, gated at 90° | $R_{DCO}$ |
|---|---|---|---|---|
| 233* | 361 | 89(11) | 91 (10) | 0.97(0.22) |
| 520* | | | | |
| 686* | 233 | 37(13) | 73(20) | 0.5 (0.1) |
| 1280* | 974 | 94(17) | 89(18) | 1.0 (0.2) |
| 1660* | 233 | 33 (11) | 33(10) | 1.0 (0.3) |
| 1614* | 233 | 45(13) | 44(9) | 1.0 (0.3) |
| 899 | 497 | 3446(101) | 33544(164) | 0.972(0.076) |
| 328 | 973+899 | 4101(52) | 3456(94) | 1.18(0.03) |
| 973 | 899 | 6491(107) | 5606(88) | 1.16(0.04) |
| 361 | 919 | 509(12) | 630(23) | 0.80(0.02) |

### 5.2.2 Linear Polarization of γ-rays

The EXOGAM detectors which are explained in part 2, are convenient for Compton polarization measurements[29]. The seven detectors placed at 90° relative to the beam axis are most sensitive ones for the polarization measurements, so only these seven EXOGAM detectors were used for the analysis. Experimental polarization P is given in Sect. 4.3.2, by equation 4.14. It is related to polarization asymmetry A by:

$$A=QP \tag{5.2}$$

Where Q is the γ-ray energy dependent polarization sensitivity for the EXOGAM detectors. Q=1 would indicate fully sensitive and Q = 0 would indicate fully insensitive detectors. The Q values for EXOGAM detectors are found in Zheng and de France research. [8].In order to determine the asymmetry degree "A" for γ rays, two new γ-γ matrices were prepared. The x-axis of these matrices include all γ-ray energies whereas the Y-axis contain the γ rays that are scattered parallel or perpendicular to the beam axis. Total projections of these matrices are shown in Fig. 5.7(a) and (b). The experimental asymmetry is defined by the formula:

$$A=\frac{\left(a_n n(perp.)-n(paral.)\right)}{\left(a_n n(perp.)+n(paral.)\right)}. \tag{5.3}$$

Here, n (perp) and n (paral) are the peak areas for specific γ-ray transitions in parallel and perpendicular scattered gamma ray spectra. The normalization factor for asymmetry, $a_n$, depends on EXOGAM clover detectors and γ-ray energy:

$$a_n(E_\gamma)=\frac{N_{\mathrm{II}}(unpolarized)}{N_{\perp}(unpolarized)}. \tag{5.4}$$

Whit the experimental $^{152}$Eu radioactive source data, the normalization factor was formulized as:

$$a_n = a_0 + a_1 E_\gamma\ , \tag{5.5}$$

and the constants $a_0$=1.05(3) and $a_1$ = 3.9(9) x$10^{-5}$ were calculated in the research done by Zheng. [8]

In the interpretations, one can need a limits for taking as a reference. For the reference values theoretical formula given in Section 4.3.2 is used. If the A (asymmetry parameter) is negative then the transition is stretched magnetic, else it is stretched electric. And if it is around zero, then the transition is a possible admixture of electric and magnetic transitions. Also, stretched E1, E2 and nonstreched M1 has an opposite signs as compared to stretched M1 and nonstreched E1.

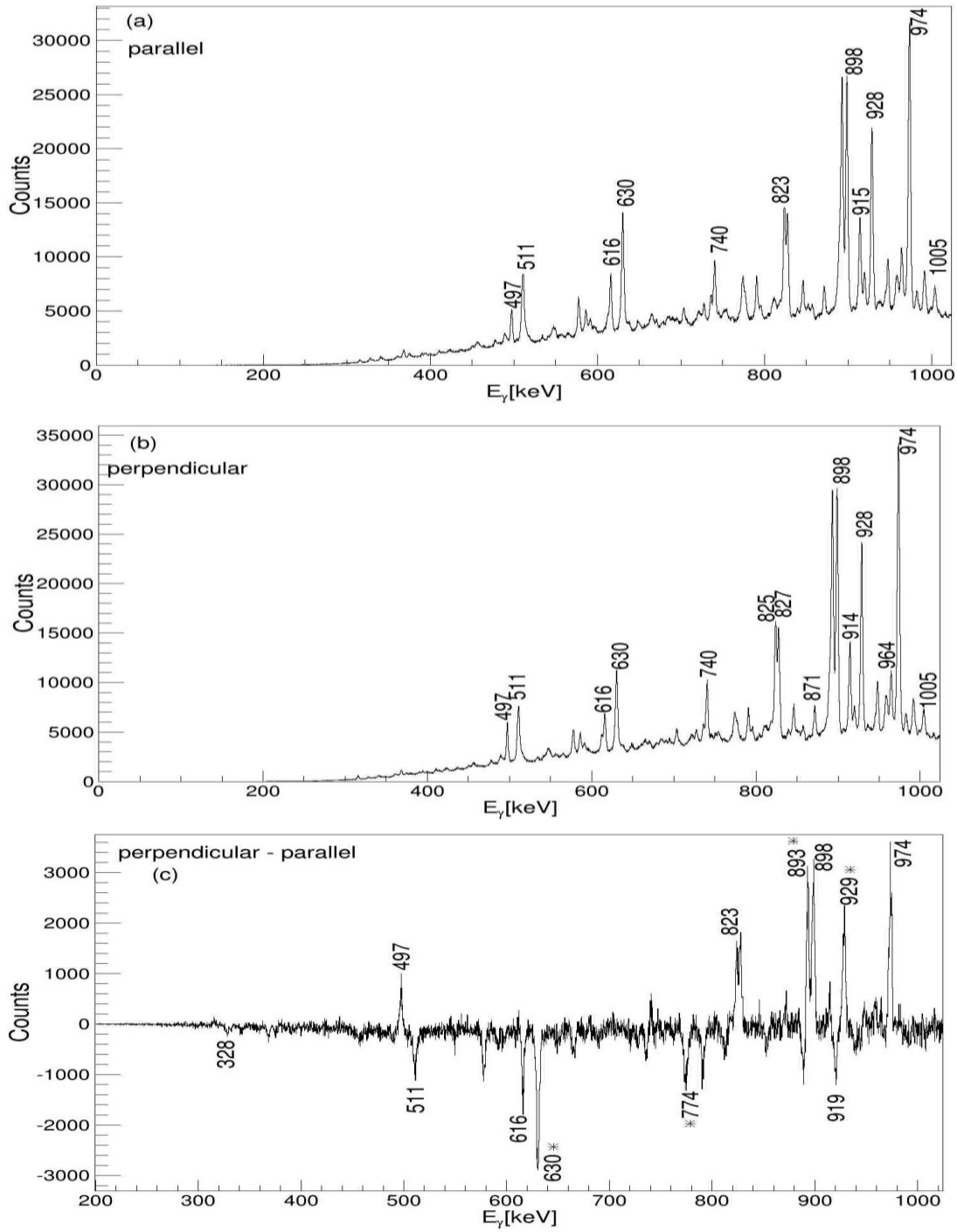


Figure 5.8: Spectra of (a) parallel and (b) perpendicular Compton scattered γ rays. The spectrum (c) is obtained by subtracting (a) from (b). Since the 91Ru channel is one of the strongest channel, the polarization studies were made without any particle or neutron gate.$^{91}$Tc peaks are shown by *.

Fig. 5.8(c) was obtained by subtracting the histogram shown in Fig. 5.8(a) from Fig. 5.8(b). The well-known, lowest lying transitions at 974 keV and 898 keV are seen as positive peaks in Fig. 5.8(c) in agreement with their stretched E2 character, whereas the 616 keV transitions appears as a negative peak in agreement with a stretched M1 character. As this spectrum is no particle gated spectrum, other strong channel 3p $^{91}$Tc peaks can be seen. For example 775 keV, 828 keV, and 630 keV are known transitions in $^{91}$Tc and their known electromagnetic nature [30] agrees with the results of Fig. 5.8 (c).

Experimentally determined polarization asymmetry (A) values with $R_{DCO}$ values are listed in Table 5.3. The results are summarized in a two dimensional plot in fig. 5.9. Where the $R_{DCO}$ values, obtained by gating on a known quadrupole transition, are shown as a function of A.

Table 5.3: Experimental Asymmetry and $R_{DCO}$ values.

| $E_\gamma$ | Asymmetry | $R_{DCO}$ | gate |
|---|---|---|---|
| 686* | -0,018(0,005) | 0,5(0,2) | 973 |
| 1005 | 0,1(0,05) | 1,02(0,1) | 973 |
| 974 | 0,096(0,005) | 1,16(0,037) | 899 |
| 965 | 0,06(0,007) | 0,95(0,2) | 871 |
| 919 | -0,12 (0,013) | 0,99(0,09) | 973 |
| 898 | 0,1(0.003) | 0,972(0,076) | 974 |
| 777 | -0,05(0,017) | 0,71(0,25) | 973 |
| 727 | -0,072(0,019) | 0,89(0,057) | 871 |
| 616 | -0,12(0,006) | 0,66(0,062) | 497 |
| 516 | 0,17(0,02) | 0,98(0,2) | 973 |
| 391 | -0,26(0,076) | 0,66(0,15) | 973 |
| 361 | -0,31(0,15) | 0,77(0,1) | 973 |
| 328 | -0,39 (0,057) | 1,18(0,05) | 973 |
| 300 | -0,2(0,015) | 0,86(0,14) | 973 |

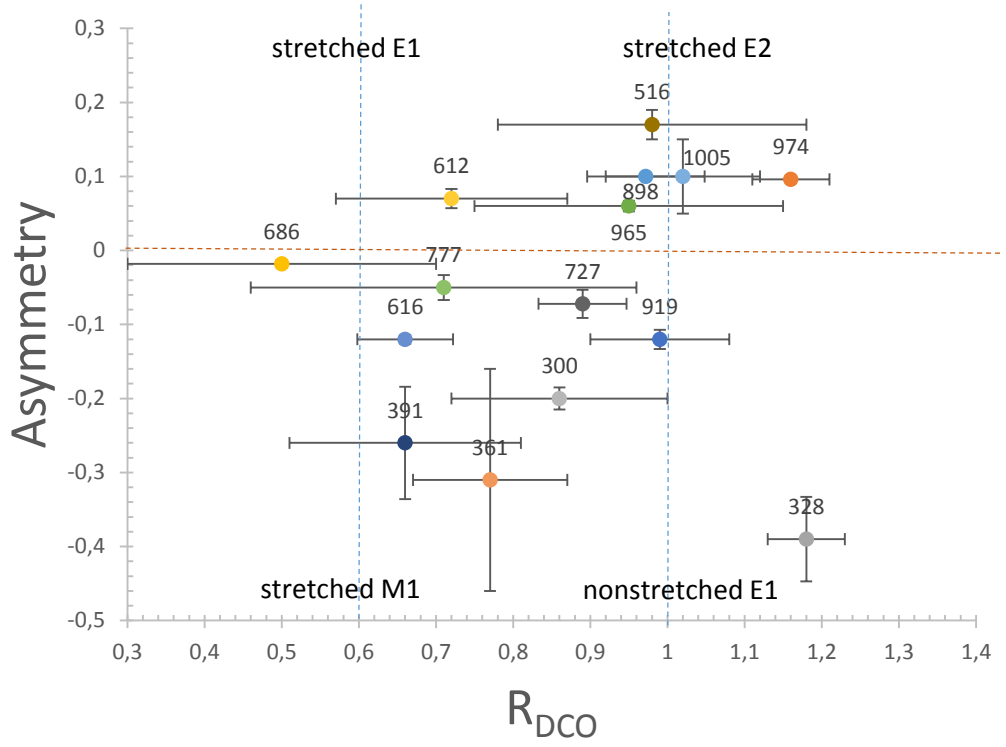


Figure 5.9: Two dimensional plot of the Asymmetry ratio versus the DCO ratio of selected γ-rays which are belong to $^{91}$Ru. Stretched E1, E2 and M1 and nonstreched E1 areas are marked in the plot and the blue dashed lines which indicate pure stretched dipole and quadrupole transitions are drawn to guide the eye.

Fig. 5.9 shows that the well-known γ-ray transitions at 974 keV has a stretched E2 character. Since the ground state of $^{91}$Ru is assumed to be $(9/2^+)$, one can conclude that this transition originates from an excited state at an energy of 974 keV and spin $(13/2^+)$, in agreement with the earlier results [6, 7]. The 898 keV transition also has an E2 character and it connects the 1872 keV $(17/2^+)$ state with the 974 keV $(13/2^+)$ state, again in agreement with the earlier results. The most interesting transitions in the $^{91}$Ru level scheme are the ones that are expected to connect the (-) parity states to the (+) parity ones. These transitions, for example at 919 keV and 328 keV, indicate nonstreched E1 character, confirming the earlier results [6, 7].

Apart from the lowest lying transitions, several others were studied in order to confirm the earlier spin and parity assignments. As it can be seen in Fig.5.9, the 965 keV, 956 keV, 516 keV and 1005 keV transitions clearly show a stretched E2 character in agreement with the spin and parity assignments of Arnell and Hesse. The transitions at 328keV and 919keV connect the (-) parity $17/2^-$ and $13/2^-$ states to the (+) parity $17/2^+$ and $13/2^+$ states in the level scheme give in Fig. 5.6. As expected, they reveal a nonstreched E1 character in Fig. 5.9. The stretched M1 character of 727keV, 391 keV 361keV, 616 keV and 777 keV transitions shown in Fig, 5.9, also agree with the earlier assignments.

An A value for the newly observed 686 keV transition was determined as -0.018, which indicates a stretched M1 character in Fig. 5.9. In the level scheme of $^{91}$Ru, Fig. 5.6, the 686 keV transition was located between the newly observed 1660 keV state and the 974 keV ($13/2^+$) state. By making use of the stretched M1 character of the 686 keV transition, one can suggest that the spin and parity of the 1660 keV state should be ($11/2^+$). In order to make firm assignment, one also needs to know the A values for the 233 keV, 1614 keV and 1660 keV transitions which originate from the 1660 keV state. Due to low statistics and low detector efficiency at low and high γ-ray energies, A values for the newly observed 233keV, 1280 keV , 1614 keV and 1660 keV transitions, could not be determined.

For the new transitions 234 keV, 1660keV, 1614 keV, 1280 keV, one can make tentative multipolarity determination just taking reference as $R_{DCO}$ values, without asymmetry values. Although this method doesn't give a firm results, before this experiment Arnell and Hesse didn't use the asymmetry values to define spin and parity of levels. Therefore from the $R_{DCO}$ values the interpretations can be done as follows:

For obtaining the $R_{DCO}$ value for the 234 keV transition, the 361 keV transition gate was used, as shown in Table 5.2. From the asymmetry measurements, Fig. 5.9, the 361 keV transition has a stretched M1 character. From the $R_{DCO}$ reference values given in Sect. 5.1.1, we know that, if the gate is a dipole transition then the $R_{DCO}$ value should be around 1.0 for a stretched dipole transition. Therefore, the 234 keV transition is a dipole transition, because its $R_{DCO}$ value is 0.97. The 234 keV transition can be E1 or M1 transition depending on the parity changes. Since the 234 keV transition is emitted from the known 1893 keV ($13/2^-$ ) state, it should decay into a 1660keV (11/2) state. This result agrees well with the discussions above where the spin and parity of the 1660 keV state was assigned to ($11/2^+$). In this case, the 234 keV transition should be of E1 type to change parity.

The 234 keV gate was used for the 1660 keV transition, and the $R_{DCO}$ value was determined to be 1.0, which means that is dipole transitions. From the level scheme in Fig. 5.8, one can see that 1660 keV transition is in between the 1660 keV ($11/2^+$) state and the ground state. Since there is no parity change between these two states, the1660 keV transition should be of stretched M1 type.

The $R_{DCO}$ values for the 1280 keV and 1614 keV transitions do not give clear results, which may be due to bad statistics and contaminations from other reaction channels in the spectra. As stated before, it is important to determine the A values before drawing firm conclusions.

# CHAPTER 6

## SUMMARY AND CONCLUSIONS

In this thesis, the γ-ray transitions from the $^{91}$Ru nucleus are studied in order to obtain information about the structure of this nucleus. $^{91}$Ru has 44 protons and 47 neutrons, and is located close to the proton drip line. It is a slightly deformed transitional nucleus and it is a good example for testing the NSM. In previous studies [7, 8], the experimental results were indeed compared to the NSM calculations and good agreement was obtained.

The experiment was performed at the GANIL facility in 2010 and it continued for 14 days. In order to reach the nucleus $^{91}$Ru, heavy-ion fusion evaporation reaction was used with a $^{58}$Ni target and an $^{36}$Ar beam at an energy of 111MeV. The beam was delivered by the Spiral accelerator system at GANIL. For charged particle detection DIAMANT detector system and for neutron detection N-Wall detector system was used. The γ-ray transitions were measured by the EXOGAM Ge detectors. The $^{91}$Ru daughter nucleus was produced after 1n and 2p evaporation from the compound nucleus $^{94}$Pd.

The level scheme of $^{91}$Ru was known from earlier experimental studies [6, 7], however, their spin and parity assignments were tentative based on the angular correlation studies. In this work, both angular correlation and linear polarization measurements were performed. For angular correlation measurements $R_{DCO}$ method was used. With the unique design of the EXOGAM γ-ray detectors, it was possible to make polarization measurements by using the Compton scattering of γ-rays. This method was not tried before on this nucleus. Unlike angular correlation measurements, by making polarization measurements one can determine whether the radiation is electric or magnetic in nature, and in this way achieve firm spin and parity assignments for the nuclear states.

The first step of this research was determining the new γ ray transitions which belong to $^{91}$Ru nucleus. Six new γ-ray transitions were observed and placed in the level scheme of $^{91}$Ru, during this thesis work. These are the 234 keV, 520 keV, 686 keV, 1280 keV, 1614 keV and 1660 keV transitions. These transitions and 12 more are published and compared to the shell model predictions of ref. [8]. In order to determine the spins and parities of the known and new transitions, the $R_{DCO}$ and Linear Polarization methods were used in the second step of this study. As a result of this measurement, the multipolarities of γ-ray transitions were determined and new spin and parity values were assigned to the nuclear states. One new excited state was observed at the energy of 1660 keV and its spin and parity were determined to be $(11/2)^+$. For the known states, the previous spin and parity assignments were confirmed.

## REFERENCE LIST


[1] M. Mlađenović, The History of Early Nuclear Physics: 1896 - 1931, World Scientific Publishing Company Incorporated, 1992.

[2] W. Nazarewicz, Nuclear Structure at the Limits, in: Eleventh Physics Summer School on Frontiers in Nuclear Physics: From Quark-Gluon Plasma to Supernova, Canberra, Australia, 1998.

[3] R.F. Casten, New Physics With Radioactive Beams: Exotic Structures in Loosely Bound Systems, Journal of Physics G: Nuclear and Particle Physics, 25 (1999) 747.

[4] S.M. Lenzi, F. Nowacki, A. Poves, K. Sieja, Island of Inversion Around $^{64}$Cr, Physical Review C, 82 (2010) 054301.

[5] B. Cederwall, F.G. Moradi, T. Bäck, A. Johnson, J. Blomqvist, E. Clément, G. De France, R. Wadsworth, K. Andgren, K. Lagergren, Evidence for A Spin-Aligned Neutron-Proton Paired Phase From the Level Structure of $^{92}$Pd, Nature, 469 (2010) 68-71.

[6] S.E. Arnell, D. Foltescu, H.A. Roth, Ö. Skeppstedt, A. Nilsson, S. Mitarai, J. Nyberg, First Information About the Level Structure of $^{91}$Ru, Physica Scripta, 47 (1993) 355.

[7] J. Heese, H. Grawe, K.H. Maier, R. Schubart, F. Cristancho, C.J. Gross, A. Jungclaus, K.P. Lieb, D. Rudolph, J. Eberth, S. Skoda, High Spin States and Shell Model Description of the Neutron Deficient Nuclei $^{90}$Ru and $^{91}$Ru, Physical Review C, 49 (1994) 1896-1903.

[8] Y. Zheng, G. de France, E. Clément, A. Dijon, B. Cederwall, R. Wadsworth, T. Bäck, F.G. Moradi, G. Jaworski, B.M. Nyakó, J. Nyberg, M. Palacz, H. Al-Azri, G. de Angelis, A. Atac, **Ö. Aktaş**, S. Bhattacharyya, T. Brock, P.J. Davies, A. Di Nitto, Z. Dombradi, A. Gadea, J. Gal, P. Joshi, K. Juhasz, R. Julin, A. Jungclaus, G. Kalinka, J. Kownacki, G. La Rana, S.M. Lenzi, J. Molnar, R. Moro, D.R. Napoli, B.S.N. Singh, A. Persson, F. Recchia, M. Sandzelius, J.N. Scheurer, G. Sletten, D. Sohler, P.A. Söderström, M.J. Taylor, J. Timar, J.J. Valiente-Dobon, E. Vardaci, Gamma-Ray Linear Polarization Measurements and $(g_{9/2})^{-3}$ Neutron Alignment in $^{91}$Ru, Physical Review C, 87 (2013) 10.

[9] W. Gelletly, J. Eberth, Gamma-Ray Arrays: Past, Present and Future, in: J. Al-Khalili, E. Roeckl (Eds.) The Euroschool Lectures on Physics with Exotic Beams, Vol. II, Springer Berlin Heidelberg, 2006, pp. 79-134.

[10] S. Gales, The GANIL Facility, Scholarpedia, 5 (2010) 9670.

[11] F. Chautard, GANIL Operation Status and Developments, in: CYCLOTRONS 2010, Chinese Academy of Sciences, Lanzhou, China, 2010, pp. 16-20.

[12] F. Ghazi Moradi, In-Beam Spectroscopy of the Neutron Deficient Nuclei $^{92}$Pd and $^{162}$Ta, in, KTH, 2011.

[13] Ö. Skeppstedt, H. Roth, L. Lindström, R. Wadsworth, I. Hibbert, N. Kelsall, D. Jenkins, H. Grawe, M. Gorska, M. Moszyński, The EUROBALL Neutron Wall–Design and Performance Tests of Neutron Detectors, Nuclear Instruments and Methods in Physics Research Section A: Accelerators, Spectrometers, Detectors and Associated Equipment, 421 (1999) 531-541.

[14] D. Radford, RadWare analys program package, in, Oak Ridge National Laboratory, Physics Division, 2000.

[15] V. Devanathan, Nuclear Physics, Alpha Science International, India, 2011.

[16] W. Greiner, J. Maruhn, Microscopic Models, in: Nuclear Models, Springer Berlin Heidelberg, 1996, pp. 207-292.

[17] J.-L. Basdevant, Fundamentals in Nuclear Physics: From Nuclear Structure to Cosmology, Springer, 2005.

[18] K.S. Krane, Introductory Nuclear Physics, John Wiley & Sons, Australia, 1988.

[19] P. Moller, J.R. Nix, W.D. Myers, W.J. Swiatecki, Nuclear Ground-State Masses and Deformations, Atomic Data and Nuclear Data Tables, 59 (1995) 185-381.

[20] P. Komninos, E. Nolte, P. Blasi, The level scheme of $^{91}$Tc and the β decay of $^{91}$Ru ($9/2^{+}$), Z Physik A, 314 (1983) 135-142.

[21] M.F. L'Annunziata, 1 - Nuclear Radiation, Its Interaction with Matter and Radioisotope Decay, in: F.L.A. Michael (Ed.) Handbook of Radioactivity Analysis (Second Edition), Academic Press, San Diego, 2004, pp. 1-121.

[22] G.F. Knoll, Radiation Detection and Measurement, Wiley. com, 2010.

[23] H. Morinaga, T. Yamazaki, In-beam gamma-ray spectroscopy, (1976).

[24] T. Yamazaki, Tables of Coefficients for Angular Distribution of Gamma Rays from Aligned Nuclei, in, Univ. of California, Berkeley, 1967.

[25] P. Twin, W. Olsen, D. Sheppard, Polarization and Angular Correlation Measurements Following the $^{40}$Ar (p, nγ) $^{40}$K Reaction, Nuclear Physics A, 143 (1970) 481-496.

[26] G. Mukherjee, A.A. Sonzogni, Nuclear Data Sheets for A = 88, Nuclear Data Sheets, 105 (2005) 419-556.

[27] M.R. Bhat, J.K. Tuli, Nuclear Data Sheets for A = 69, Nuclear Data Sheets, 90 (2000) 269-390.

[28] N.J. Weiszflog Matthias, dco_EXOGAM, in: N. Johan (Ed.), Uppsala University, 2010.

[29] G. Duchêne, F.A. Beck, P.J. Twin, G. de France, D. Curien, L. Han, C.W. Beausang, M.A. Bentley, P.J. Nolan, J. Simpson, The Clover: a New Generation of Composite Ge Detectors, Nuclear Instruments and Methods in Physics Research Section A: Accelerators, Spectrometers, Detectors and Associated Equipment, 432 (1999) 90-110.

[30] S.E. Arnell, D. Foltescu, H.A. Roth, Ö. Skeppstedt, A. Nilsson, S. Mitarai, J. Nyberg, High-spin States of the Neutron Deficient Isotope $^{91}$Tc, Physica Scripta, 47 (1993) 142.

nn